Viscoelastic-Viscoplastic Homogenization of Short Glass-Fiber Reinforced Polyamide Composites (PA66/GF) with Progressive Interphase and Matrix Damage: New Developments and Experimental Validation

Qiang Chen[a], George Chatzigeorgiou[a], Gilles Robert[b], Fodil Meraghni[a*]

[a]Arts et Métiers Institute of Technology, CNRS, Université de Lorraine, LEM3-UMR7239, F-57000 Metz, France

[b]Polytechnyl sas - Domochemicals Lyon 6919, France

*Corresponding author. Email: fodil.meraghni@ensam.eu

Date: August 24, 2021

Abstract

In this paper, an original probabilistic micromechanics damage framework involving multi-deformation mechanisms, based on the modified Mori-Tanaka and Transformation Field Analysis (MT-TFA) techniques, is developed to predict monotonic and oligocyclic stress-strain responses in short fiber-reinforced polyamide composites. The proposed model allows simulating actual injection-induced fiber arrangement, which is characterized by arbitrary fractions of randomly oriented fibers distributed in the laminate plane. Furthermore, the modified MT-TFA approach employs a phenomenological model consisting of four Kelvin-Voigt branches and a viscoplastic branch, formulated under the thermodynamics framework, to describe the rate-dependent viscoelastic-viscoplastic deformation and the ductile damage of the polymer matrix phase. In addition, the Weibull probabilistic density function is utilized to simulate initiation and coalescence of the void-type discrete damage in the vicinity of the fiber/matrix interphase, induced by the fiber/matrix debonding as observed experimentally. The parameters of the developed model are calibrated against the experimental response of glass/polyamide (PA66/GF35) composites via

uniaxial loading/unloading tests, by taking into account the actual fiber orientation density function (ODF). The reliability and efficiency of the modified Mori-Tanaka and TFA scheme are assessed vis-à-vis the separate and hold-out experimental data subjected to uniaxial and oligocyclic loading at various loading rates. Progressive matrix and interphase damage are compared in support of the modified MT-TFA technique's capabilities to capture the experimentally observed damage mechanisms. To accurately capture the experimental response, the progressive degradation of the load transfer between the fiber and matrix phases is introduced through a reduction of the active fiber length. The latter is introduced by considering the effect of the interphase void-damage content. The new mean-field formulation provides accurate predictions of the overall response under complex loading paths. It can be combined with other techniques in our future work, such as cycle-jump, towards simulating high-cycle fatigue damage in short-fiber composite structures.

Keywords: Progressive Damage; Probabilistic Density Function; Mori-Tanaka Homogenization; Transformation Field Analysis; Viscoelastic-Viscoplastic Behavior; Interphase; Orientation Density Function.

1. Introduction

Thermoplastic composites have found wide-ranging applications in various engineering technologies, such as aerospace, wind energy, marine, automotive, as well as sports equipment. They are relatively high strength and lightweight materials, besides their low processing and manufacturing costs (Wei et al., 2019). Additionally, thermoplastic composites can withstand rigorous and harsh physical as well as the chemical environment, such as moderate-high or low temperatures and corrosion, but without loss of their structural integrity. To make the best use of these materials, it is critically important to have a good understanding of their macroscopic

mechanical behaviors and the underlying damage and deformation mechanisms. Such knowledge is key to efficiently design durable and sustainable structural components to meet the specific needs of applications.

In general, characterizing the response of thermoplastic composites can be conducted either through experiments or numerical simulations. The experimental work on composites, however, can be very tedious and costly in light of a myriad of possible combinations of constituent materials, and therefore is performed only for limited material systems with a specific fiber volume fraction and microstructural configuration (Kaddour et al., 2013; Wei et al., 2020). To get a comprehensive understanding of the deformation mechanisms of thermoplastic composites, it is imperative to develop reliable numerical tools to efficiently gauge their overall stress-strain response integrating the process-induced microstructure.

The response of thermoplastic composites is influenced by a number of factors that need to be understood in the course of conducting an experimental/analytical correlation with micromechanics simulations. First of all, the fiber orientation distributions and their corresponding volume fractions are known to affect substantially the local stress fields and the overall composite response. This is particularly true in the case of the short glass fiber reinforced polyamide-66 composites (PA66/GF) investigated in this work. As reported by Arif et al. (2014a), the PA66/GF has a specific microstructure characterized by a well-defined skin-shell-core layer formation, as depicted in Figure 1, which has been frequently observed in a thin-plate structure of thermoplastic composites during the injection molding manufacturing process. Specifically, the fibers are randomly oriented in the skin layers which typically represent 5% of the plate thickness. The shell layers, whose preferential orientation direction is parallel to the mold flow direction, are the most

dominant layers, occupying about 90% of the plate thickness. The core layer fills up to 5% of the plate thickness and most fibers in this layer are oriented perpendicular to the mold flow direction.

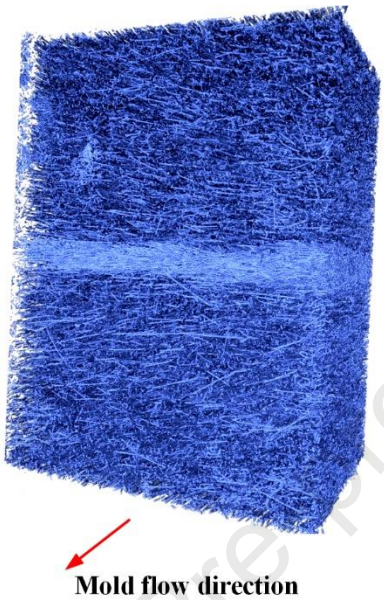

Figure 1 Skin-shell-core microstructure observed in the through-thickness of PA66/GF composites

In addition to the local process-induced microstructure, it is well recognized that the thermoplastic composites exhibit substantial time-dependent inelastic deformation, due to the creep or stress relaxation of the viscoelastic polyamide matrix. Beyond the elastic and viscoelastic limits, the polyamide matrix undergoes unrecoverable plastic deformation and a creep flow that are also time-dependent. Such deformation mechanism has been modelled using the viscoelastic-viscoplastic constitutive models in the literature (Krairi et al., 2019; Praud et al., 2017a). Therefore, to correctly simulate the macroscopic response integrating the material microstructure, the chosen micromechanics model must accommodate such a complex constitutive model at the phase level.

Another important consideration in simulating the stress-strain response of polyamide composites is the ability to admit the local damage initiation and accumulation. Indeed, under certain loading conditions, significant microcracks may grow within the composite microstructures, which eventually lead to catastrophic failure of the composite materials and

structural components. Unlike metals where the damage commonly initiates from the most stressed points and evolves over a large volume of materials, the damage mechanisms in composites are remarkably different due to the myriad of failure mechanisms and modes, and their complex nature in terms of initiation and coalescence at different scales (Huang and Talreja, 2006). A case in point is the damage evolution mechanisms in glass/polyamide (PA66/GF) composites shown in Figure 2, as reported by Arif et al. (2014a), where a number of factors are found responsible for the ultimate failure in this class of materials. Figure 2(a) shows the matrix microcracking, interface debonding and effective (or active) fiber length reduction, in the PA66/GF composites observed by the scanning electron microscope (SEM). Figures 2(b) and 2(c) show the in-situ scanning electron microscope micrographs of the 3-point bending test in the tension zone corresponding to the skin-shell region that exhibits the matrix microcracking and interface debonding at 73% and 88% ultimate stress levels respectively. These figures indicate that the presence of defects in the fiber/matrix interphase leads to extensive fiber/matrix debonding, even at very low macroscopic stresses. From an experimental point of view, the interface damage is characterized by the onset and the coalescence of voids in the vicinity of the fibers. In contrast, away from this fiber/matrix interphase region, the matrix damage is ductile, which occurs in an interaction with the viscoplasticity. Moreover, the interphase discrete damage, particularly at the fiber ends, directly reduces the active fiber length that remains attached to the matrix, hence severely altering the load-transfer capability from the matrix to the fibers as observed in Figure 2(a). The effects of interphase/interface discrete and matrix ductile damages on the stress-strain response of polyamide composites have attracted significant attention of the simulation community, Mao et al. (2021); Tu and Chen (2020); Despringre et al.(2016).

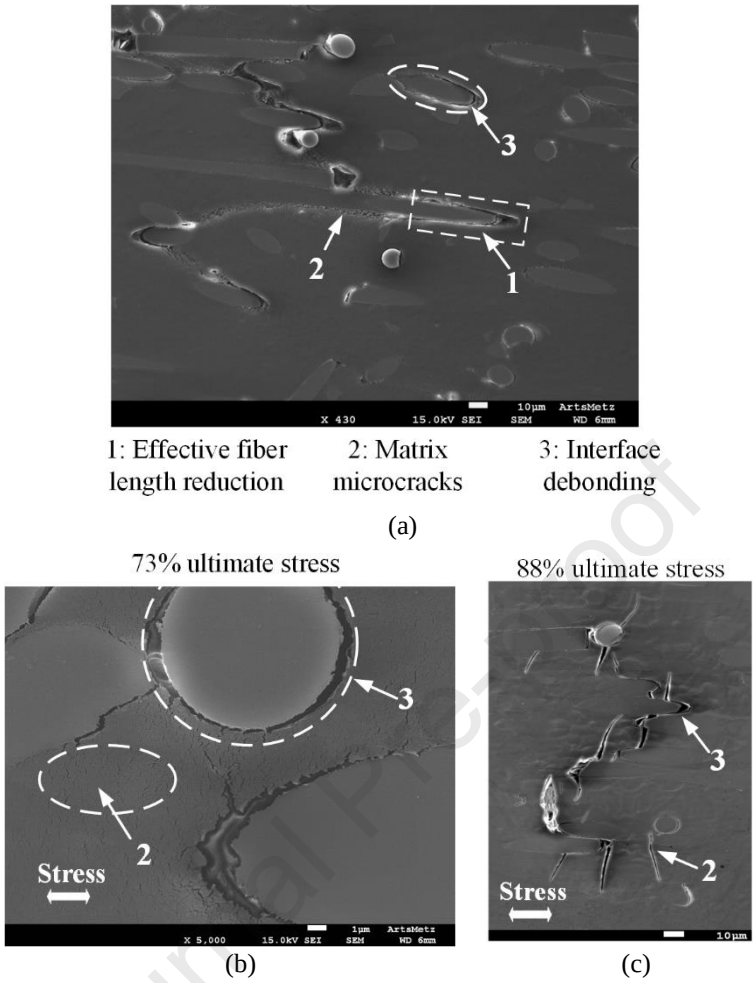

Figure 2 Damage mechanisms in short glass-fiber reinforced polyamide composites (PA66/GF) as reported by Arif et al. (2014a): (a) effective fiber length reduction, matrix microcracks and interface debonding observed experimentally; matrix microcracks and interface debonding at (b) 73% and (c) 88% ultimate stress levels observed via the in-situ SEM 3-point bending test. The observations are carried out in the tension zone (skin-shell region).

Each of the microstructure factors and damage/deformation modes outlined above has the potential to significantly affect the macroscopic stress-strain response of the composite materials. Consequently, it is essential to identify and quantify all of these mechanisms and to assess their interactions. Presently, a number of micromechanics models are available in the literature to predict the stress-strain behavior of composites. These models, in general, can be categorized into two broad categories. The first class of approaches is based on the full-field analysis, such as the finite-element (Chatzigeorgiou et al., 2016; Praud et al., 2021; Tikarrouchine et al., 2021), finite-

volume (Chen et al., 2017; Tu and Chen, 2020), asymptotic (Cruz-González et al., 2020; Otero et al., 2020; Rodríguez-Ramos et al., 2012), locally-exact (Drago and Pindera, 2008; He and Pindera, 2021), mesh-free (Chen and Aliabadi, 2019), and fast Fourier transformation (Lahellec and Suquet, 2007; Moulinec and Suquet, 1998) homogenization of composite materials containing elastic, viscoelastic, viscoplastic, and damage phases. The full-field analysis approaches are suitable for modelling detailed microstructures but require substantial effort for the input data construction. Simulating three-dimensional microstructures is a challenging issue as it needs a great deal of computing power and can be incredibly slow. This aspect may prevent them from being efficiently used in the parametric studies aiming at understanding the structural integrity-property relationship. The second class of methods is the classical or extended mean-field homogenization methods, such as the self-consistent method (Mercier and Molinari, 2009), the generalized self-consistent method (Hine and Gusev, 2019), the Mori-Tanaka method (Barral et al., 2020; Barthélémy et al., 2019; Peng et al., 2016; Song et al., 2020), and the bridging micromechanics (Huang and Huang, 2020; Huang, 2020; Huang et al., 2021b), which are based on Eshelby's well-established equivalence principle (Eshelby, 1957). Other developments of the mean-field approaches include the variational-incremental (Boudet et al., 2016; Brassart et al., 2012; Lahellec and Suquet, 2007) or incremental-secant (Wu et al., 2013) models. These advanced models are based on the introduction of a linear comparison composite and the computation of the first and second statistical moments. Relative to the full-field analysis, the classical or extended mean-field approaches provide closed-form constitutive equations for combined thermo-mechanical multi-axial loading without the need for computationally-demanding three-dimensional unit cell analysis. As a result, the computation time of the mean-field approaches is reduced by at least an order relative to the full-field analysis.

The readers are referred to the review articles by Charalambakis et al. (2018) and Chen et al. (2018) for additional references in this area.

The potential benefits that may be obtained from the use of polyamide composites have led to an increasing interest in understanding deformation and failure mechanisms in this class of materials. Launay et al. (2011) established a phenomenological model for simulating the cyclic behavior of short glass fiber reinforced polyamide, which described the short and long-term viscoelasticity, nonlinear viscous flow, and cyclic softening. Tu and Chen (2020) developed finite-volume-based micromechanics with interface damage modelled using the cohesive zone model. The nonlinear stress-strain response of graphite/polyamide composites is simulated based on the hypothesis of shear-dominated fiber/matrix interfacial degradation as the primary cause of the observed nonlinearity. Ammar et al. (2021) developed a discrete element approach to simulate interfacial debonding process modelling using the cohesive zone model in short glass-fiber-reinforced composites, in particular the PA6/GF30 composites. Huang et al. (2021a) proposed a bridging micromechanics model for predicting the failure strength of aligned and randomly oriented short fiber composites. They derived the closed-form expressions for the concentration factors to covert the homogenized stresses of the matrix into the true values such that predicting failure strength can be made using only the original constituent strength data with good accuracy.

The novelty of the present work is to capture the rate-dependent stress-strain behavior of short glass fiber reinforced polyamide composites under monotonic and oligocyclic loading by taking into account physically justified deformation and damage mechanisms, including viscoelasticity, viscoplasticity, interphase decohesion, and matrix ductile damage, as well as integrating the actual injection-induced fiber orientation distributions. To the best of the authors' knowledge, thus far, there has been no reported work of micromechanical methods on the

nonlinear short glass fiber reinforced polyamide composites with such complex behavior under oligocyclic loading in the literature.

Herein, a modified Mori-Tanaka Transformation Field Analysis approach developed by Chen et al. (2021a), for unidirectional composites undergoing progressive damage coupled with viscoelastic-viscoplastic deformation, is further extended and extensively validated to address the short-fiber reinforced composites with random fiber orientation. The new approach is capable of considering the fiber orientation density function. The latter can be obtained experimentally through X-Ray micro-computed tomography investigation (Hessman et al., 2019) or estimated through the orientation tensors, which are extracted from the injection process simulation (Advani and Tucker, 1987; Müller and Böhlke, 2016). The developed model integrates the injection-process fiber orientation distribution, hence enabling a more realistic simulation of the composite response. Furthermore, the matrix constitutive behavior is simulated using a phenomenological viscoelastic-viscoplastic ductile damage model, developed under the thermodynamics framework by Praud et al. (2017a), while the interphase discrete microcracks/voids are described by the Weibull probabilistic function for debonding initiation and evolution. The new contributions of the present work include:

- The modified Mori-Tanaka and TFA framework developed by Chen et al. (2021a) has been further extended for accommodating the rate-dependent stress-strain response of randomly oriented short fiber composites.
- The new approach takes into account the actual injection-induced fiber arrangement and experimentally observed damage and deformation modes/mechanisms of the PA66/GF composites.

- Demonstration of the reasonable accuracy of the developed micromechanics framework, given the complexity of the overall response, against the experimental results for short fiber reinforced polyamide composites under uniaxial monotonic and oligocyclic loading conditions.

It should be pointed out the basic framework of the present MT-TFA approach follows the idea of the three-phase Mori-Tanaka approach, originally developed by Chatzigeorgiou and Meraghni (2019) and Barral et al. (2020) considering inelastic fields in the absence of damage. According to that work, the interphase is introduced into the classical Mori-Tanaka approach to take into account the excessive stress concentration in the elastic-plastic region of the interphase. In the present work, the interphase plays an additional role of simulating the discrete damage arising from the fiber-matrix debonding. The progressive reduction of the active fiber length evidenced in experiments can be directly related to the interface damage as well.

The remainder of the present work is organized as follows: Section 2 presents the theoretical framework of the probabilistic MT- TFA approach with random fiber orientations. Section 3 introduces the phase constitutive models and their numerical implementations. Section 4 identifies the parameters of the model against the experimental response of glass/polyamide composites under the uniaxial loading/unloading path. Section 5 demonstrates the predictive capabilities of the developed model for simulating the inelastic response of short-fiber reinforced polyamide composites under complex oligocyclic loading conditions as well as the overall apparent stiffness reduction. Discussion and further development of the proposed technique is presented in section 6. Section 7 draws the pertinent conclusions.

2. Theoretical Development

2.1 Modified Mori-Tanaka TFA Approach for Unidirectional Composites

A brief overview of the extended Mori-Tanaka-based TFA framework is recalled for unidirectional fiber-reinforced composites accounting for interphase discrete damage and matrix ductile damage. Full development of the technique is referred to the work by Chen et al. (2021a).

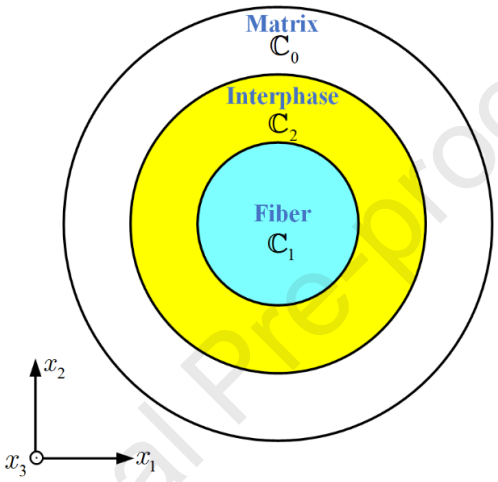

Figure 3 A three-phase Mori-Tanaka model with progressive interphase and void damage

The extended Mori-Tanaka approach is based on the transformation field analysis proposed by Dvorak (1992) and Dvorak and Benveniste (1992). For a three-phase composite consisting of the fiber (referred to subscript 1), the interphase (referred to subscript 2), and the matrix (referred to subscript 0) phases, as illustrated in Figure 3, the average strain $\boldsymbol{\varepsilon}_r$ of the rth phase reads:

$$\boldsymbol{\varepsilon}_r = \mathbf{T}_r : \boldsymbol{\varepsilon}_0 + \mathbf{T}_{r0}^{in} : \boldsymbol{\varepsilon}_0^{in} + \mathbf{T}_{r1}^{in} : \boldsymbol{\varepsilon}_1^{in} + \mathbf{T}_{r2}^{in} : \boldsymbol{\varepsilon}_2^{in} \tag{1}$$

where $r = 1, 2$. $\boldsymbol{\varepsilon}_0$ denotes average matrix strain. $\boldsymbol{\varepsilon}_r^{in}$ represents the inelastic strain of the rth phase. $\mathbf{T}_r$ and $\mathbf{T}_{rp}^{in}$ $(p = 0,1,2)$ are the fourth-order elastic and inelastic interaction tensors given by (Chatzigeorgiou and Meraghni, 2019):

$$
\begin{aligned}
&\mathbf{T}_1 = \left[\varphi\mathbf{N}_{10} + (1-\varphi)\mathbf{N}_{20} : \mathbf{N}_{12}\right]^{-1}, && \mathbf{T}_2 = \mathbf{N}_{12} : \mathbf{T}_1 \\
&\mathbf{T}_{10}^{in} = -\mathbf{T}_1 : \mathbf{P}_0 : \mathbf{C}_0, && \mathbf{T}_{11}^{in} = \mathbf{T}_1 : \left[\varphi\mathbf{P}_0 + (1-\varphi)\mathbf{N}_{20} : \mathbf{P}_2\right] : \mathbf{C}_1, \\
&\mathbf{T}_{12}^{in} = (1-\varphi)\mathbf{T}_1 : \left[\mathbf{P}_0 - \mathbf{N}_{20} : \mathbf{P}_2\right] : \mathbf{C}_2, && \mathbf{T}_{20}^{in} = \mathbf{N}_{12}\mathbf{T}_{10}^{in}, \\
&\mathbf{T}_{21}^{in} = \mathbf{N}_{12}\mathbf{T}_{11}^{in} - \mathbf{P}_2 : \mathbf{C}_1, && \mathbf{T}_{22}^{in} = \mathbf{N}_{12}\mathbf{T}_{12}^{in} + \mathbf{P}_2 : \mathbf{C}_2
\end{aligned} \tag{2}
$$

where c_r denotes the volume fraction of the rth phase. φ is the fiber and interphase volume ratio: $\varphi = c_1/(c_1 + c_2)$. $\mathbf{C}_0$, $\mathbf{C}_1$, and $\mathbf{C}_2$ are the secant moduli of the matrix, fiber, and interphase, respectively. Moreover,

$$
\begin{aligned}
&\mathbf{N}_{10} = \mathbf{I} + \mathbf{P}_0 : \left[\mathbf{C}_1 - \mathbf{C}_0\right], \\
&\mathbf{N}_{20} = \mathbf{I} + \mathbf{P}_0 : \left[\mathbf{C}_2 - \mathbf{C}_0\right], \\
&\mathbf{N}_{12} = \mathbf{I} + \mathbf{P}_2 : \left[\mathbf{C}_1 - \mathbf{C}_2\right], \\
&\mathbf{P}_0 = \mathbf{S}\left(\mathbf{C}_0\right) : \mathbf{C}_0^{-1}, \\
&\mathbf{P}_2 = \mathbf{S}\left(\mathbf{C}_2\right) : \mathbf{C}_2^{-1}
\end{aligned} \tag{3}
$$

$I_{ijkl} = \left(\delta_{ik}\delta_{jl} + \delta_{il}\delta_{jk}\right)/2$ is the fourth-order identity tensor. δ_{ij} is the Kronecker delta. $\mathbf{S}\left(\mathbf{C}_0\right)$ and $\mathbf{S}\left(\mathbf{C}_2\right)$ are the Eshelby tensors (Eshelby, 1957) expressed in terms of the matrix and interphase secant moduli and the geometry of the fiber, respectively. In the case of infinitely long cylindrical fibers embedded in an isotropic matrix, an explicit expression for the Eshelby tensor may be found in the literature (Mura, 1987). Otherwise, the Eshelby tensor must be evaluated numerically using the technique developed by Gavazzi and Lagoudas (1990).

2.2 Modified Mori-Tanaka TFA Approach with Multiple Fiber Orientations: New Development

To account for multiple coated fiber orientations in a matrix, the equations in the previous subsection must be further extended and reformulated. For an *N*-orientation coated fiber composite, Eq. (1) can be rewritten in a more general manner for the *i*th fiber with its *i*th coating as follows:

$$\boldsymbol{\varepsilon}_r^i = \mathbf{T}_r^i : \boldsymbol{\varepsilon}_0 + \mathbf{T}_{r0}^i : \boldsymbol{\varepsilon}_0^{in} + \mathbf{T}_{r1}^{i,i} : \boldsymbol{\varepsilon}_1^{in,i} + \mathbf{T}_{r2}^{i,i} : \boldsymbol{\varepsilon}_2^{in,i} \tag{4}$$

where $i = 1,...,N$. $\mathbf{T}_r^i$ $(r = 1,2)$ are the elastic interaction tensors of the ith fiber and ith coating, respectively. $\mathbf{T}_{rp}^i$ $(p = 0,1,2)$ are the inelastic interaction tensors, with the superscript "*in*" omitted for the sake of simplicity. The expressions for the elastic and inelastic interaction tensors are given by analogous relations with the previous subsection. The macroscopic or the effective strain of an *N*-phase composite is expressed as a weighted sum of the average strains over all phases:

$$\overline{\boldsymbol{\varepsilon}} = c_0 \boldsymbol{\varepsilon}_0 + \sum_{i=1}^{N} \left[c_1^i \boldsymbol{\varepsilon}_1^i + c_2^i \boldsymbol{\varepsilon}_2^i \right] \tag{5}$$

Using Eq. (4) in the definition of the composite overall strain, Eq. (5), we obtain:

$$\begin{aligned} \overline{\boldsymbol{\varepsilon}} = & \left[c_0 \mathbf{I} + \sum_{i=1}^{N} \left[c_1^i \mathbf{T}_1^i + c_2^i \mathbf{T}_2^i \right] \right] : \boldsymbol{\varepsilon}_0 + \sum_{i=1}^{N} \left[c_1^i \mathbf{T}_{10}^i + c_2^i \mathbf{T}_{20}^i \right] : \boldsymbol{\varepsilon}_0^{in} \\ & + \sum_{i=1}^{N} \left[c_1^i \mathbf{T}_{11}^{i,i} + c_2^i \mathbf{T}_{21}^{i,i} \right] : \boldsymbol{\varepsilon}_1^{in,i} + \sum_{i=1}^{N} \left[c_1^i \mathbf{T}_{12}^{i,i} + c_2^i \mathbf{T}_{22}^{i,i} \right] : \boldsymbol{\varepsilon}_2^{in,i} \end{aligned} \tag{6}$$

where c_1^i and c_2^i are the volume fractions of the ith fiber and ith coating, respectively. c_0 is the matrix volume fraction computed by: $c_0 = 1 - \sum_{i=1}^{N} (c_1^i + c_2^i)$. From Eq. (6), the matrix strain can be obtained as follows:

$$\boldsymbol{\varepsilon}_0 = \mathbf{A}_0 : \overline{\boldsymbol{\varepsilon}} + \mathbf{A}_{00} : \boldsymbol{\varepsilon}_0^{in} + \sum_{i=1}^{N} \mathbf{A}_{01}^i : \boldsymbol{\varepsilon}_1^{in,i} + \sum_{i=1}^{N} \mathbf{A}_{02}^i : \boldsymbol{\varepsilon}_2^{in,i} \tag{7}$$

with

$$\begin{aligned}
\mathbf{A}_0 &= \left[c_0\mathbf{I} + \sum_{i=1}^{N} \left[c_1^i \mathbf{T}_1^i + c_2^i \mathbf{T}_2^i \right] \right]^{-1} \\
\mathbf{A}_{00} &= -\mathbf{A}_0 : \sum_{i=1}^{N} \left[c_1^i \mathbf{T}_{10}^i + c_2^i \mathbf{T}_{20}^i \right] \\
\mathbf{A}_{01}^i &= -\mathbf{A}_0 : \sum_{i=1}^{N} \left[c_1^i \mathbf{T}_{11}^{i,i} + c_2^i \mathbf{T}_{21}^{i,i} \right] \\
\mathbf{A}_{02}^i &= -\mathbf{A}_0 : \sum_{i=1}^{N} \left[c_1^i \mathbf{T}_{12}^{i,i} + c_2^i \mathbf{T}_{22}^{i,i} \right]
\end{aligned} \tag{8}$$

Substituting Eq. (7) into Eq. (4) yields:

$$\begin{aligned}
\boldsymbol{\varepsilon}_1^i &= \mathbf{A}_1^i : \bar{\boldsymbol{\varepsilon}} + \mathbf{A}_{10} : \boldsymbol{\varepsilon}_0^{in} + \sum_{j=1}^{N} \mathbf{A}_{11}^{j,i} : \boldsymbol{\varepsilon}_1^{in,j} + \sum_{j=1}^{N} \mathbf{A}_{12}^{j,i} : \boldsymbol{\varepsilon}_2^{in,j} \\
\boldsymbol{\varepsilon}_2^i &= \mathbf{A}_2^i : \bar{\boldsymbol{\varepsilon}} + \mathbf{A}_{20} : \boldsymbol{\varepsilon}_0^{in} + \sum_{j=1}^{N} \mathbf{A}_{21}^{j,i} : \boldsymbol{\varepsilon}_1^{in,j} + \sum_{j=1}^{N} \mathbf{A}_{22}^{j,i} : \boldsymbol{\varepsilon}_2^{in,j}
\end{aligned} \tag{9}$$

where

$$\begin{aligned}
&\mathbf{A}_1^i = \mathbf{T}_1^i : \mathbf{A}_0, \\
&\mathbf{A}_{10}^i = \mathbf{T}_1^i : \mathbf{A}_{00} + \mathbf{T}_{10}^i \\
&\mathbf{A}_{11}^{j,i} = \begin{cases} \mathbf{T}_1^i : \mathbf{A}_{01}^i + \mathbf{T}_{11}^{i,i} & j = i \\ \mathbf{T}_1^i : \mathbf{A}_{01}^i & j \neq i \end{cases} \\
&\mathbf{A}_{12}^{j,i} = \begin{cases} \mathbf{T}_1^i : \mathbf{A}_{02}^i + \mathbf{T}_{12}^{i,i} & j = i \\ \mathbf{T}_1^i : \mathbf{A}_{02}^i & j \neq i \end{cases}
\end{aligned} \tag{10}$$

$$\begin{aligned}
&\mathbf{A}_2^i = \mathbf{T}_2^i : \mathbf{A}_0, \\
&\mathbf{A}_{20}^i = \mathbf{T}_2^i : \mathbf{A}_{00} + \mathbf{T}_{20}^i \\
&\mathbf{A}_{21}^{j,i} = \begin{cases} \mathbf{T}_2^i : \mathbf{A}_{01}^i + \mathbf{T}_{21}^{i,i} & j = i \\ \mathbf{T}_2^i : \mathbf{A}_{01}^i & j \neq i \end{cases} \\
&\mathbf{A}_{22}^{j,i} = \begin{cases} \mathbf{T}_2^i : \mathbf{A}_{02}^i + \mathbf{T}_{22}^{i,i} & j = i \\ \mathbf{T}_2^i : \mathbf{A}_{02}^i & j \neq i \end{cases}
\end{aligned} \tag{11}$$

The macroscopic secant modulus of the composites $\mathbf{C}^*$ is then expressed in terms of phase volume fractions, secant stiffness matrices, and elastic concentration tensors as follows:

$$\mathbf{C}^{*} = c_0\mathbf{C}_0\mathbf{A}_0 + \sum_{i=1}^{N}\left[c_1^i\mathbf{C}_1^i : \mathbf{A}_1^i + c_2^i\mathbf{C}_2^i : \mathbf{A}_2^i\right] \tag{12}$$

2.3 Model Formulation Accounting for Random Orientations with Finite Fiber Length

Theoretically, there is no specific number of inclusions that can be determined in an absolute manner. A composite with randomly oriented fibers, in theory, has fibers in all possible orientations. However, it is possible to identify an orientation density function that defines a probability for each orientation to appear. A common composite that appears frequently in the automotive industry consists of a matrix reinforced with fibers and the fibers are distributed in random orientation. Automotive structures exhibit three-dimensional fiber orientations, leading to an ODF described by two orientation angles (Zhu et al., 1997). Assume that fibers and coatings have a total volume fraction of c_1 and c_2, respectively, and the fiber and interphase volume ratio φ is kept the same at every orientation. For a general case, if ϕ denotes the angle of orientation with respect to $\bar{x}_3$ axis and ζ denotes the out of plane angle of orientation with respect to $\bar{x}_1$ axis, Eq. (12) can be written as:

$$\begin{aligned}\mathbf{C}^{*} = c_0\mathbf{C}_0\mathbf{A}_0 + c_1\int_{-\pi}^{\pi}\int_{-\frac{\pi}{2}}^{+\frac{\pi}{2}} g(\phi,\zeta)\mathbf{C}_1(\phi,\zeta)\,\mathbf{A}_1(\phi,\zeta)\sin\phi\,\mathrm{d}\phi\,\mathrm{d}\zeta \\ + c_2\int_{-\pi}^{\pi}\int_{-\frac{\pi}{2}}^{+\frac{\pi}{2}} g(\phi,\zeta)\mathbf{C}_2(\phi,\zeta)\sin\phi\,\mathbf{A}_2(\phi,\zeta)\,\mathrm{d}\phi\,\mathrm{d}\zeta\end{aligned} \tag{13}$$

where $g(\phi,\zeta)$ denotes the fiber orientation density function in the case fibers are distributed in all possible directions in the three-dimensional space, and $\int_{-\pi}^{+\pi}\int_{-\pi/2}^{+\pi/2} g(\phi,\zeta)\sin\phi\,\mathrm{d}\phi\,\mathrm{d}\zeta = 1$. In the case the function $g(\phi,\zeta)$ is a constant, there is an equal probability of appearance of all

orientations. When the function $g(\phi,\zeta)$ has an analytical expression, the scalar integral of Eq. (13) can be computed exactly.

For structural components produced in the form of the thin plate (the thickness ranging between $1\,mm$ and $4mm$), however, the fiber orientation angles ζ with respect to the out-of-plane axis $\bar{x}_1$ are very small (Arif et al., 2014b). As consequence, the micromechanics analysis in the present work is performed considering the fibers distributed randomly on the $\bar{x}_2-\bar{x}_3$ plane, Figure 4(a), and the fiber orientation density function is characterized by just one angle ϕ, Figure 4(b). In such case, Eq. (12) can be rewritten as:

$$\begin{aligned}\mathbf{C}^{*} = c_0\mathbf{C}_0\mathbf{A}_0 + c_1\int_{-\frac{\pi}{2}}^{+\frac{\pi}{2}} g(\phi)\mathbf{C}_1(\phi)\mathbf{A}_1(\phi)\,\mathrm{d}\phi \\ + c_2\int_{-\frac{\pi}{2}}^{+\frac{\pi}{2}} g(\phi)\mathbf{C}_2(\phi)\mathbf{A}_2(\phi)\,\mathrm{d}\phi\end{aligned} \tag{14}$$

where $g(\phi)$ denotes the fiber orientation density function in the case fibers are randomly distributed on a plane, and $\int_{-\pi/2}^{+\pi/2} g(\phi)\mathrm{d}\phi = 1$. The initial fiber length l in the composites can be either finite or infinite, depending on the manufacturing process and geometry of the constituent fibers (Launay et al., 2011). The averaged fiber aspect ratio determined via the experiment for an actual composite is employed in the present work.

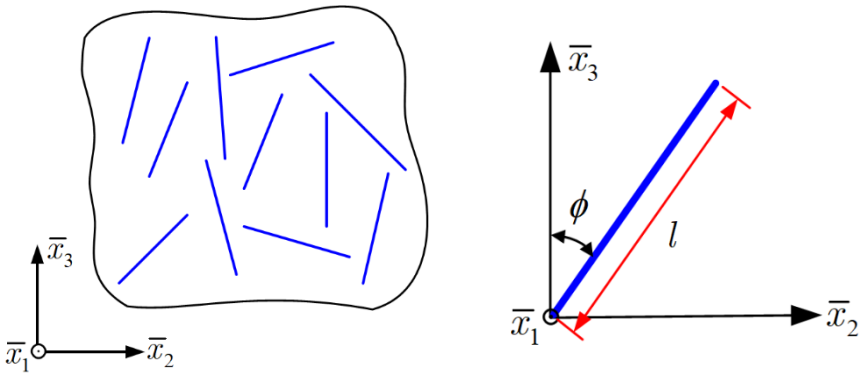

(a) (b)

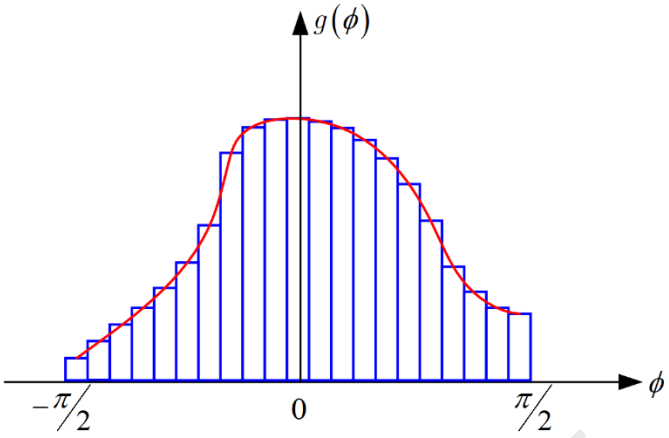

(c)

Figure 4 (a) Illustration of short-fiber reinforced composites with random fiber orientation; (b) The relative position of a fiber rotated by an angle of ϕ with respect to $\overline{x}_3$ axis on the $\overline{x}_2 - \overline{x}_3$ plane; (c) Approximation of the orientation density function using rectangles of constant width

In order to keep the comprehensive structure of Eq. (12), which is also more suitable for numerical implementation, the integral is approximated using the rectangles of constant step. Considering N discrete orientations, Figure 4(c), the step h becomes π/h . The macroscopic secant modulus of the N-orientation composites reads:

$$\mathbf{C}^* = c_0\mathbf{C}_0\mathbf{A}_0 + \frac{\pi}{N}\sum_{i=1}^{N}\left[c_1 g(\phi_i)\mathbf{C}_1^i : \mathbf{A}_1^i + c_2 g(\phi_i)\mathbf{C}_2^i : \mathbf{A}_2^i\right] \tag{15}$$

3. Numerical Implementation

Apart from the micromechanics scheme, the accurate characterization of the composite homogenized behaviors relies on a sophisticated constitutive law that describes the stress increments for the given strain increments at each phase. In this present work, the randomly oriented composites consist of three constituent materials. The inclusion phase is glass fibers which are assumed to be linearly elastic during the entire loading history. The matrix is the PA66 polyamide that exhibits viscoelastic-viscoplastic behavior with ductile damage. The interphase surrounding fibers consists of a PA66 polyamide, which is characterized using the viscoelastic-

viscoplastic model with void creation. For the readers' convenience, the essential information about the matrix and interphase constitutive laws is summarized below. A full exposition of those phase models can be found in previous publications (Chen et al., 2021a; Praud et al., 2017a).

3.1 Constitutive Law for the Matrix

Semi-crystalline polymers are known to exhibit substantial time-dependent inelastic stress-strain behavior and accordingly have been modelled using viscoelastic-viscoplastic formalism. In particular, the inelastic strains $\boldsymbol{\varepsilon}_0^{in}$ appearing on right-hand sides of Eqs. (7) and (9) are integrated using the viscoelastic-viscoplastic (VE-VP) constitutive equation developed by Praud et al. (2017a) based on an appropriate thermodynamic principle, under the infinitesimal deformation assumption and isothermal conditions. Moreover, these materials are assumed to experience a gradual stiffness degradation during the loading/unloading due to the initiation and growth of matrix microcracks. The damage mechanisms in the matrix phase can be characterized through continuum damage theory based on the well-known principle of effective stress introduced by Lemaitre and Chaboche (1994).

The rheological model for the matrix phase can be described using *N* Kelvin-Voigt branches and a viscoplastic branch positioned in series, as illustrated in Figure 5. Under the thermodynamics framework, the Helmholtz free energy for the matrix medium reads:

$$\begin{aligned}\rho\psi\left(\boldsymbol{\varepsilon},\boldsymbol{\varepsilon}_{vi},\boldsymbol{\varepsilon}_{vp},r,d\right)=&\frac{1}{2}\left(\boldsymbol{\varepsilon}-\sum_{i=1}^{N}\boldsymbol{\varepsilon}_{vi}-\boldsymbol{\varepsilon}_{vp}\right):\left(1-d\right)\mathbf{C}_e:\left(\boldsymbol{\varepsilon}-\sum_{i=1}^{N}\boldsymbol{\varepsilon}_{vi}-\boldsymbol{\varepsilon}_{vp}\right)\\&+\frac{1}{2}\sum_{i=1}^{N}\boldsymbol{\varepsilon}_{vi}:\left(1-d\right)\mathbf{C}_{vi}:\boldsymbol{\varepsilon}_{vi}+\int_0^p R\left(\xi\right)d\xi\end{aligned}\tag{16}$$

where $\mathbf{C}_e$ (representing the initial matrix stiffness tensor $\mathbf{C}_0$) and $\mathbf{C}_{vi}$ denote the elastic stiffness tensor and the viscoplastic tensor of the ith branch, respectively. $\boldsymbol{\varepsilon}$, $\boldsymbol{\varepsilon}_{vi}$, and $\boldsymbol{\varepsilon}_{vp}$ are total,

viscoelastic, and viscoplastic strains, respectively. d denotes the ductile matrix damage variable represented as a scalar quantity. R is the hardening function.

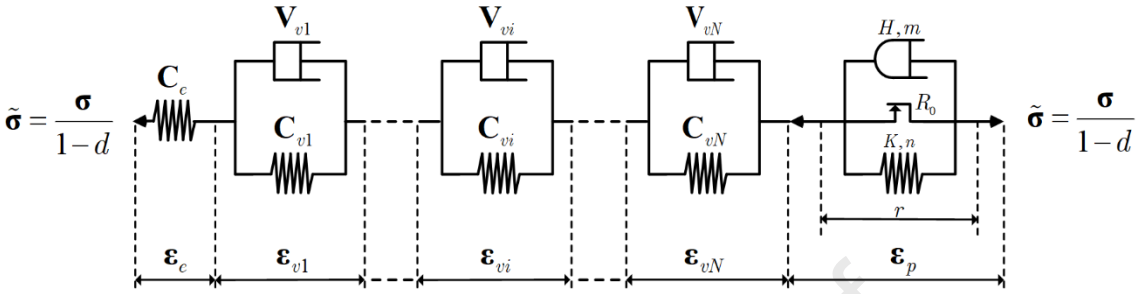

Figure 5 Rheological scheme of the VE-VP-d (Praud et al., 2017a) adopted for the polyamide matrix

The associated thermodynamic variables are obtained from the derivation of the potential with respect to their corresponding state variables, which are summarized in Table 1, where $\mathbf{V}_{vi}$ are the fourth-order viscous tensors, $\boldsymbol{\sigma}_{vi}$ are the viscoelastic stresses, dev($\boldsymbol{\sigma}$) designates the deviatoric stresses, eq($\boldsymbol{\sigma}$) is the equivalent von Mises stress.

Table 1 Summary of the constitutive relations for the VE-VP-d matrix phase

State variables	Associated variables	Evolution law
Observable state variable		
Total strain $\boldsymbol{\varepsilon}$	$\boldsymbol{\sigma} = \rho \frac{\partial \psi}{\partial \boldsymbol{\varepsilon}}$	-
Internal state variable		
Viscoelastic strain $\boldsymbol{\varepsilon}_{vi}$	$-\boldsymbol{\sigma}_{vi} = \rho \frac{\partial \psi}{\partial \boldsymbol{\varepsilon}_{vi}}$	$\dot{\boldsymbol{\varepsilon}}_{vi} = \mathbf{V}_{vi}^{-1} : \boldsymbol{\sigma}_{vi}$
Viscoplastic strain $\boldsymbol{\varepsilon}_p$	$-\boldsymbol{\sigma} = -\rho \frac{\partial \psi}{\partial \boldsymbol{\varepsilon}_p}$	$\dot{\boldsymbol{\varepsilon}}_p = \frac{3}{2} \frac{dev(\boldsymbol{\sigma})}{(1-d)eq(\boldsymbol{\sigma})} \dot{p}$
Accumulated plastic strain p	$R(p) = \rho \frac{\partial \psi}{\partial p}$	$\dot{p} = \dot{\lambda}$
Accumulated damage d	$Y = -\rho \frac{\partial \psi}{\partial d}$	$\dot{d} = \frac{1}{(1-d)} \left[\frac{Y}{S} \right]^{\beta} \dot{\lambda}$

3.2 Constitutive Law for the Interphase

The interphase is assumed to possess the same material as the matrix phase before undergoing the void initiation and coalescence. Therefore, the inelastic rheological behavior of the interphase follows the same VE-VP constitutive law as that of the matrix phase. The Mori-Tanaka method, however, is based on the average stress per phase. Hence, it significantly overestimates the macroscopic stress-strain response in the elastic-plastic region, if not the homogenized elastic moduli. It is also noted from the full-field analysis that the interphase surrounding the matrix accumulates substantial inelastic deformation that affects the post-yield stress-strain response. On this basis, the stress overshoot is corrected by the inelastic strains in the interphase layers which are directly linked to the matrix strain through a correction tensor $\mathbf{Y}$, as proposed by Barral et al. (2020):

$$\boldsymbol{\varepsilon}_2^{in} = \mathbf{Y} : \boldsymbol{\varepsilon}_0^{in} \tag{17}$$

For a short fiber-reinforced composite with fiber oriented in $\bar{x}_3$ direction, the correction tensor may be expressed in the following form:

$$\mathbf{Y} = \begin{bmatrix} \gamma^N & 0 & 0 & 0 & 0 & 0 \\ 0 & \gamma^N & 0 & 0 & 0 & 0 \\ 0 & 0 & \gamma^L & 0 & 0 & 0 \\ 0 & 0 & 0 & \gamma^{ST} & 0 & 0 \\ 0 & 0 & 0 & 0 & \gamma^{SL} & 0 \\ 0 & 0 & 0 & 0 & 0 & \gamma^{SL} \end{bmatrix} \tag{18}$$

In the above equation, γ^N, γ^L, γ^{ST}, and γ^{SL} denote the difference between matrix and interphase inelastic strains in transverse normal, longitudinal, transverse shear, and axial shear directions, respectively following the local coordinate system in Figure 3.

Conversely to the matrix damage which occurs in a rather slowly processing manner, the damage in the vicinity of the fiber is characterized by sudden occurrence and coalescence of voids or defects, which is supported by the experimental microscopic observations for short glass fiber reinforced polyamide composites (Arif et al., 2014a). This is supposed to be an outcome of the high-stress concentration due to the large fiber/matrix property mismatch (contrast) and the manufacturing defects during the consolidation process that commonly appear in this region.

The void accumulation in the interphase layers is described using the stiffness reduction, which is depicted by a fourth-order tensor $\mathbf{D}(\gamma_c)$ that recessively degrades the initial stiffness tensor of the interphase $\mathbf{C}_2$ occupying this layer, Figure 6, cf. Praud et al. (2017b); Chen et al. (2021a). It is recalled that the interphase's initial elastic stiffness is $\mathbf{C}_2 = \mathbf{C}_0$. The interphase stiffness reduction tensor $\mathbf{D}(\gamma_c)$ is then expressed as a function of interphase void volume fraction γ_c, representing the microcrack density, by assuming scale separation between the voids and the overall interphase layer. Following the Mori-Tanaka homogenization, the overall interphase stiffness of the equivalent interphase medium reads:

$$\mathbf{C}_2(\gamma_c) = \mathbf{C}_0 - \mathbf{D}(\gamma_c) = (1-\gamma_c)\mathbf{C}_0 : \mathbf{A}_m(\gamma_c) \tag{19}$$

where $\mathbf{A}_m(\gamma_c)$ is the strain concentration tensor of the net matrix embedding voids. The strain concentration tensor $\mathbf{A}_m(\gamma_c)$ is directly computed using the two-phase Mori-Tanaka model:

$$\mathbf{A}_m(\gamma_c) = \mathbf{T}_m : \left[(1-\gamma_c)\mathbf{T}_m + \gamma_c \mathbf{T}_c\right]^{-1} \tag{20}$$

with $\mathbf{T}_m = \mathbf{I}$, $\mathbf{T}_c = \left[\mathbf{I} - \mathbf{S}(\mathbf{C}_0)\right]^{-1}$ and $\mathbf{S}(\mathbf{C}_0)$ denotes the Eshelby tensor determined by the stiffness tensor of the net matrix surrounding the voids and the ellipsoidal geometry of the voids.

The final expression of the overall interphase stiffness with void creation and growth is obtained by substituting Eq. (20) into Eq. (19):

$$\mathbf{C}_2\left(\gamma_c\right)=\mathbf{C}_0-\mathbf{D}\left(\gamma_c\right)=\mathbf{C}_0-\gamma_c\mathbf{C}_0:\mathbf{T}_c:\mathbf{A}_m\left(\gamma_c\right) \tag{21}$$

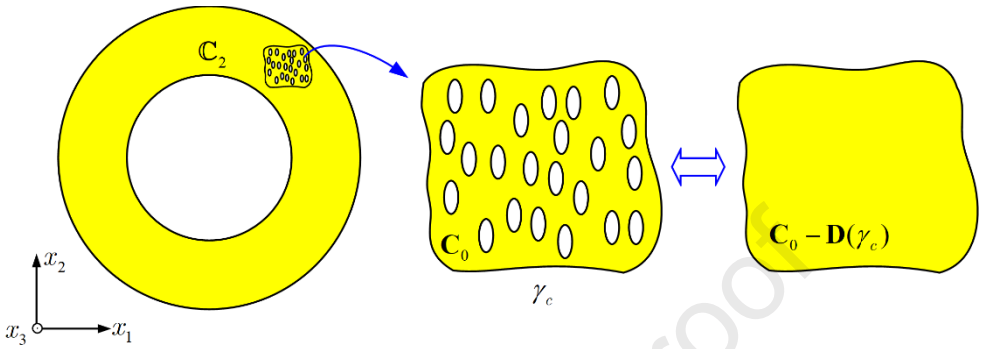

Figure 6 Discrete void-type damage in the interphase represented by the microcrack density γ_c. The secant modulus $\mathbf{C}_2$ of the homogenized interphase is evaluated in terms of the net matrix modulus $\mathbf{C}_0$ and microcrack density γ_c

Depending on the fiber/matrix bonding state of particular interphase, the void initiation and accumulation in the interphase can occur even at very low stresses, which may significantly affect the load-bearing capability of the composite materials. The void growth in the interphase region can be modelled using a Weibull probabilistic density function (Desrumaux et al., 2000; Weihull, 1951) that is commonly used in the micromechanics-based models to characterize various types of damage evolution. The cumulative probability function of the interphase void content reads:

$$\gamma_c=\gamma_{\max}\left(1-\exp\left(-\left[\frac{\left\langle\bar{\sigma}_2^{eff}-\sigma_a\right\rangle}{\sigma_c}\right]^{\kappa}\right)\right) \tag{22}$$

In the above equation, $\gamma_{\max}$ represents the saturation limit of the microcrack density such that $\gamma_c\le\gamma_{\max}$. $\bar{\sigma}_2^{eff}$ denotes the homogenized interphase effective stress. σ_c and κ are the Weibull parameters, the combination of which controls how rapid interphase microcrack may grow. σ_a denotes the damage threshold stress activating the microcrack initiation in the interphase. $\langle\ \rangle$

indicates the Macaulay bracket. Figure 7(a) illustrates the effect of the Weibull exponent κ on the interphase void growth in the case of $\sigma_c = 50$ MPa , $\sigma_a = 0$ MPa , and $\gamma_c = 1$. As observed, for small κ cases, the interphase void damage is activated at very low stresses and the microcrack density increases with the effective interphase macroscopic stress but with a diminishing rate. For large κ cases, a lower probability of interphase microcrack is expected at the initial stage of the deformation. The interphase microcrack formation, however, may occur abruptly when the effective stress approaches the critical stress $\sigma_c = 50$ MPa , indicating a catastrophic failure of the interphase. Figure 7(b) illustrates the effect of critical stress σ_c on the interphase void growth when the Weibull exponent κ is held constant as 0.5. It is clearly shown that decreasing σ_c substantially promotes the interphase void growth.

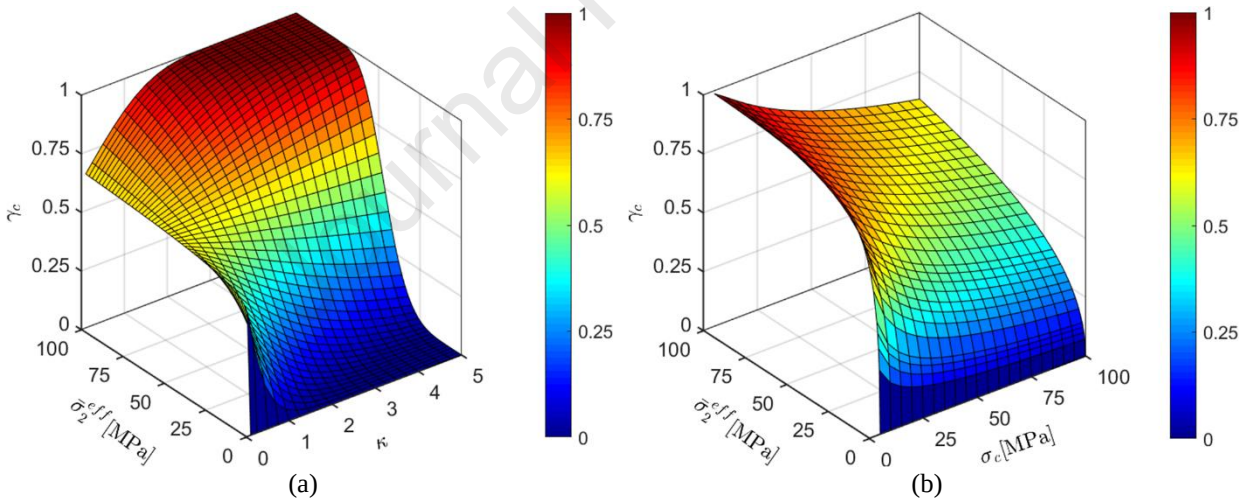

Figure 7 (a) Illustration of the effect of Weibull exponent κ on the interphase void growth in the case of constant $\sigma_c = 50$ MPa ; (b) effect of critical stress σ_c on the interphase void growth in the case of constant $\kappa = 0.5$

3.3 Interphase Damage Induced Progressive Effective Fiber Length Reduction

The initiation and growth of the interphase microcracks near the fiber ends significantly alter the stress-transfer mechanisms between the fibers and the supporting matrix. The load transfer occurs thus only in the residual active fiber length that remains attached to the matrix, namely, the non-

debonded portion. As a result, the effective (or active) fiber length, which plays a vital role in controlling the load-bearing capability in the short-fiber composites, may also decrease progressively with increasing interphase voids due to the interphase decohesion. The effective fiber length l can be expressed as a function of the interphase damage progressive degradation, namely, the interphase microcrack density γ_c. Herein, the effective fiber length l is linked to γ_c in simple form:

$$l = L_0\left(1-\alpha\gamma_c\right) \tag{23}$$

where L_0 denotes the initial fiber length. α is the parameter controlling how fast the effective fiber length reduction may be activated. For simplicity, α has been kept as 1 in generating results that follow. The effective fiber length reduction can take into account the effect of interphase discrete damage on the stress-transfer mechanisms between the fibers and the supporting matrix in this class of materials, enabling more accurate characterization of the stress-strain behavior via the modified Mori-Tanaka approach with random fiber orientations.

3.4 Iterative Strategy

The modified Mori-Tanaka TFA approach with randomly oriented fibers is implemented using the secant stiffness matrix approach based on the return mapping algorithm (Chatzigeorgiou et al., 2018; Simo and Hughes, 1998). The homogenized constitutive equation can be expressed as:

$$\bar{\boldsymbol{\sigma}} = \mathbf{C}^{*}\bar{\boldsymbol{\varepsilon}} - \bar{\boldsymbol{\sigma}}^{in} \tag{24}$$

where $\mathbf{C}^{*}$ is the homogenized secant stiffness matrix of the randomly oriented fiber-reinforced composites given by Eq. (12) or the Eq. (15), based on the secant stiffness tensors of the matrix $\mathbf{C}_0 = (1-d)\mathbf{C}_0$, fiber $\mathbf{C}_1 = \mathbf{C}_1$, and the interphase $\mathbf{C}_2 = \mathbf{C}_0 - \mathbf{D}\left(\gamma_c\right)$, $\mathbf{C}_0$ and $\mathbf{C}_1$ are the initial elastic stiffness tensors of the matrix and fiber phase, respectively. For a given macroscopic strain

increment, the stress overshoot is corrected through the inelastic stresses $\bar{\boldsymbol{\sigma}}^{in}$. The convergence of the numerical procedure is obtained till either the difference of the macroscopic strains between two successive iterations is within a specified tolerance or the iterations reach a prescribed number. It should be mentioned that the employed secant stiffness matrix approach is more advantageous than the tangential stiffness matrix approach typically used in the finite-element or finite-volume-based solutions (Chatzigeorgiou et al., 2016; Chen et al., 2021b) in several aspects. In particular, the former doesn't require the formulation of the tangent stiffness matrix which must be reformed many times during the Newton-Rapson iterations. In addition, the tangent stiffness matrix may become singular or ill-conditioned in the nonlinear stress-strain region, which consequently produces numerical instabilities and non-converged results. The general iterative scheme of the modified Mori-Tanaka TFA method is described in detail in Table 2.

Table 2 Iterative scheme of the modified Mori-Tanaka TFA method for composites with random fiber orientations

1. At time step n, everything is known for all the phases in both scales.

2. At the beginning of the time step $n+1$, set all the average microscopic variables, secant moduli, and the concentration tensors at every phase equal to their corresponding values at time step n. At the specific iteration, the macroscopic strain increment $\Delta\bar{\boldsymbol{\varepsilon}}$ for the composites is calculated from the homogenized Hooke's law, Eq. (24).

3. Compute the microscopic strain increment for each phase from:

$$\Delta\boldsymbol{\varepsilon}_1^i = -\boldsymbol{\varepsilon}_1^{i(n)} + \mathbf{A}_1^i : \left[\bar{\boldsymbol{\varepsilon}}^{(n)} + \Delta\bar{\boldsymbol{\varepsilon}}\right] + \mathbf{A}_{10} : \boldsymbol{\varepsilon}_0^{in} + \sum_{j=1}^{N} \mathbf{A}_{11}^{j,i} : \boldsymbol{\varepsilon}_1^{in,j} + \sum_{j=1}^{N} \mathbf{A}_{12}^{j,i} : \boldsymbol{\varepsilon}_2^{in,j}$$

$$\Delta\boldsymbol{\varepsilon}_2^i = -\boldsymbol{\varepsilon}_2^{i(n)} + \mathbf{A}_2^i : \left[\bar{\boldsymbol{\varepsilon}}^{(n)} + \Delta\bar{\boldsymbol{\varepsilon}}\right] + \mathbf{A}_{20} : \boldsymbol{\varepsilon}_0^{in} + \sum_{j=1}^{N} \mathbf{A}_{21}^{j,i} : \boldsymbol{\varepsilon}_1^{in,j} + \sum_{j=1}^{N} \mathbf{A}_{22}^{j,i} : \boldsymbol{\varepsilon}_2^{in,j}$$

$$\Delta\boldsymbol{\varepsilon}_0 = -\boldsymbol{\varepsilon}_0^{(n)} + \frac{1}{c_0}\left[\bar{\boldsymbol{\varepsilon}}^{(n)} + \Delta\bar{\boldsymbol{\varepsilon}}\right] - \frac{1}{c_0}\sum_{i=1}^{N} c_1^i \left[\boldsymbol{\varepsilon}_1^{i(n)} + \Delta\boldsymbol{\varepsilon}_1^i\right] - \frac{1}{c_0}\sum_{i=1}^{N} c_2^i \left[\boldsymbol{\varepsilon}_2^{i(n)} + \Delta\boldsymbol{\varepsilon}_2^i\right]$$

4. At every phase, evaluate the microscopic inelastic strain as well as the secant modulus using the phase constitutive law described in previous subsections. The microscopic stress per phase is then computed by:

$$\boldsymbol{\sigma}_1^i = \mathbf{C}_1 : \left[\boldsymbol{\varepsilon}_1^{i(n)} + \Delta\boldsymbol{\varepsilon}_1^i \right] = \mathbf{C}_1 : \left[\boldsymbol{\varepsilon}_1^{i(n)} + \Delta\boldsymbol{\varepsilon}_1^i \right]$$

$$\boldsymbol{\sigma}_2^i = \mathbf{C}_2^i : \left[\boldsymbol{\varepsilon}_2^{i(n)} + \Delta\boldsymbol{\varepsilon}_2^i - \boldsymbol{\varepsilon}_2^{in,i} \right] = \left[\mathbf{C}_0 - \mathbf{D}\left(\gamma_c\right) \right]^i : \left[\boldsymbol{\varepsilon}_2^{i(n)} + \Delta\boldsymbol{\varepsilon}_2^i - \mathbf{Y} : \boldsymbol{\varepsilon}_0^{in} \right]$$

$$\boldsymbol{\sigma}_0 = \mathbf{C}_0 : \left[\boldsymbol{\varepsilon}_0^{(n)} + \Delta\boldsymbol{\varepsilon}_0 - \boldsymbol{\varepsilon}_0^{in} \right] = (1-d)\mathbf{C}_0 : \left[\boldsymbol{\varepsilon}_0^{(n)} + \Delta\boldsymbol{\varepsilon}_0 - \boldsymbol{\varepsilon}_0^{in} \right]$$

5. Evaluate the concentration tensors at every phase, according to Eqs. (8), (10) and (11).

6. Check the local convergence of the average strain per phase. If the phase strain ceases to change then continue with step 7, otherwise return to step 3.

7. Compute the macroscopic stress and the macroscopic inelastic stress:

$$\bar{\boldsymbol{\sigma}} = c_0\boldsymbol{\sigma}_0 + \sum_{i=1}^{N} \left[c_1^i \boldsymbol{\sigma}_1^i + c_2^i \boldsymbol{\sigma}_2^i \right]$$

$$\bar{\boldsymbol{\sigma}}^{in} = \bar{\boldsymbol{\sigma}} - \mathbf{C}^* : \left[\bar{\boldsymbol{\varepsilon}}^{(n)} + \Delta\bar{\boldsymbol{\varepsilon}} \right]$$

8. Check the global convergence criterion. If the global convergence of macroscopic strain is satisfied then go to the next macroscopic strain increment, otherwise return to step 2.

4. Identification of the Interphase Parameters

In this section, the extended Mori-Tanaka TFA framework is employed to describe the uniaxial loading/unloading and oligocyclic stress-strain response of short fiber-reinforced composites at different loading rates. The simulated response is validated extensively against the experimental response under various off-axis configurations.

The first investigated composite is the thermoplastic short glass fiber-reinforced polyamide (PA66/GF35) composite containing 35% fiber weight content, corresponding to 18.5% fiber volume fraction. The matrix is modelled by a phenomenological model consisting of four Kelvin-Voigt branches and a viscoplastic branch model, with damage characterized by the gradual stiffness degradation. Identification of such complex constitutive laws for the polyamide matrix, where multiple mechanisms are simultaneously involved, typically requires a complex methodology (Praud et al., 2017a). Very often it is impossible to completely isolate a single mechanism in order to identify independently its related parameters. Consequently, the

identification of matrix parameters necessitates the use of appropriate reverse engineering methods. In the present work, the matrix properties listed in Table 3 are directly taken from Praud et al. (2021). These parameters are identified by calibrating the constitutive model (VE-VP-d) predictions against the monotonic tensile, incremental load/unload tensile, and incremental load/relaxation/unload/relaxation tensile tests on the pure polyamide 6-6 using an optimization algorithm. The readers are referred to Praud et al. (2017a; 2021) for more complete references.

The glass fiber is assumed to be linearly elastic during the entire loading history, the elastic properties of which are listed in Table 3. The fiber orientation density function for the PA66/GF35 is obtained by the microcomputer tomography scan, and the measured fiber aspect ratio is 22 on average. It is important to point out that the polyamide and polyamide composites are known to be highly sensitive to the environmental condition, in particular, the relative humidity (RH) and the working temperature T . Herein, the room temperature $T = 23^{o}\mathrm{C}$ is considered whereas the relative RH is equal to 50%.

Table 3 Identified material parameters used in the random Mori-Tanaka TFA simulation ($T = 23^{o}\mathrm{C}$, RH=50%)

	Glass Fiber	Polyamide Interphase	Polyamide Matrix
E	72.4 GPa	2731 MPa	2731 MPa
υ	0.22	0.3	0.3
E_{v1}		8766 MPa	8766 MPa
η_{v1}		1395 MPa s	1395 MPa s
E_{v2}		13754 MPa	13754 MPa
η_{v2}		165601 MPa s	165601 MPa s
E_{v3}		15010 MPa	15010 MPa
η_{v3}		457955 MPa s	457955 MPa s
E_{v4}		11634 MPa	11634 MPa
η_{v4}		1307516 MPa s	1307516 MPa s
R_0		4.86 MPa	4.86 MPa
K		1304.33 MPa	1304.33 MPa
n		0.674	0.674
H		47.35 MPa s	47.35 MPa s^m
m		0.068	0.068

S		21.607
β		-1.105
γ^L	1	
γ^N	6	
γ^{ST}	2.64	
γ^{SL}	3.7	
$\gamma_{\max}$	0.99	
κ	0.62	
σ_c	55.20 MPa	

The estimated fiber-to-interphase volume ratio obtained from the experiment is $\varphi = 0.57$. As reported by Barral et al. (2020), this value also ensures the inelastic strain concentrations in the vicinity of the fiber in a reasonable range relative to the full-field finite-element simulations. The parameters that remain to be determined are the interphase Weibull parameters σ_c, σ_a, κ, and $\gamma_{\max}$, and the inelastic strain correction tensor $\mathbf{Y}$. These parameters, however, are not directly measurable, as it is impossible to separate the interphase from the composites to perform a mechanical test on them. Consequently, the interphase parameters are calibrated from the macroscopic response of the glass/polyamide composites under uniaxial off-axis loading/unloading paths. The identification of the interphase properties is achieved by minimizing a cost function expressed by the least squares between the numerical and experimental uniaxial stress responses, σ^{num} and σ^{exp} respectively:

$$\text{ArgMin } \frac{1}{2}\sum_{k=1}^{N_p} w_k \left[\sigma_k^{num} - \sigma_k^{exp}\right]^2$$

where N_p is the number of measuring points and w_k denotes the weight for kth measuring point.

In addition, it is observed experimentally that the formation of the interphase damage in this type of material manifests itself at very low stresses, with a catastrophic interfacial separation

(Arif et al., 2014a). To be consistent with this observation and also to reduce the number of parameters to be identified, σ_a and $\gamma_{\max}$ are taken directly as 0 and 0.99. In the sequel, the remaining interphase parameters σ_c, κ, and $\mathbf{Y}$ are calibrated against uniaxial loading/unloading tests of PA66/GF35 composites at two strain rates and three loading directions. Then the suitability of the identified parameters is verified by comparing the predicted stress-strain responses against the separate and hold-out experimental data under both uniaxial and oligocyclic loading/unloading paths.

Figure 8 presents the orientation density function of the glass/polyamide (PA66/GF35) obtained experimentally by mCT technique. This orientation density function distribution is consistent with the skin-shell-core microstructure of the PA66/GF30 plate observed by the scanning electron microscope test, cf. Arif et al. (2014a), as described in Figure 1. The angular spatial resolution of the ODF during the testing is 5^{o}, hence yielding $N = 36$ coated fiber phases (Eq. (15)).

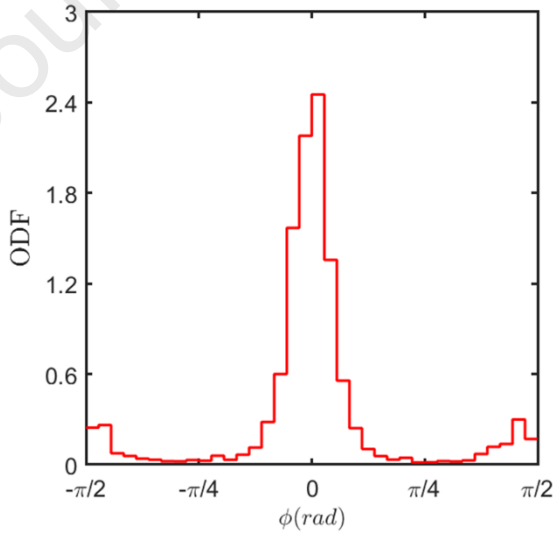

Figure 8 Experimentally measured fiber orientation density function by mCT scan investigation for PA66/GF35, showing the skin-shell-core effect

The quasi-static tensile experimental tests are first carried out on the randomly oriented PA66/GF35 glass/polyamide specimens cut from the plate with different orientations relative to the global axis, namely $\theta = 0^{o}$, 45^{o}, and 90^{o} with respect to x axis. They are loaded in the laminate plane under strain-controlled loading by the normal in-plane stress $\bar{\sigma}_{xx} \neq 0$, as illustrated in Figure 9, Moreover, in order to capture the strain rate effects, these tests are performed with a servo-hydraulic tensile machine at four different loading rates, namely, $1 \times 10^{-3}/\mathrm{s}$, $5 \times 10^{-3}/\mathrm{s}$, $1 \times 10^{-2}/\mathrm{s}$, and $5 \times 10^{-2}/\mathrm{s}$, where the axial macroscopic strain $\bar{\varepsilon}_{xx}$ is measured by an extensometer, while the axial macroscopic stress $\bar{\sigma}_{xx}$ is collected by a load cell.

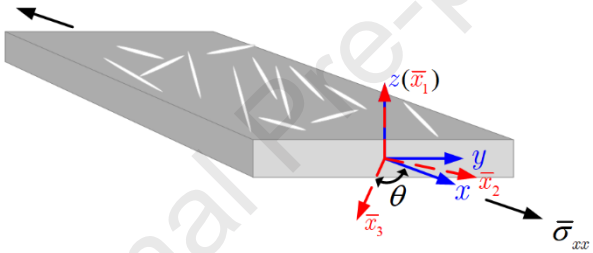

Figure 9 An off-axis specimen uniaxially loaded along the x axis in the global coordinates

The identification of the interphase parameters is achieved by minimizing a cost function containing the differences between the numerical and experimental macroscopic stresses for the 0^{o}, 45^{o}, and 90^{o} PA66/GF35 dogbone specimens with the actual dimensions given in Arif et al. (2014b). The identified interphase parameters are listed in Table 3. Figure 10 shows the calibrated stress-strain behaviors generated by the extended Mori-Tanaka methods against the experimental data, which are carried out at loading rates of $1 \times 10^{-3}/\mathrm{s}$ and $5 \times 10^{-2}/\mathrm{s}$, thus covering a wider range of loading rates. To verify the correctness of the calibrated interphase parameters, the comparison between the simulated stress-strain response and experimental values at two additional loading rates of $1 \times 10^{-2}/\mathrm{s}$ and $5 \times 10^{-3}/\mathrm{s}$. The stress-strain responses for these two loading configurations, which are not used in the identification process are shown in Figure 11. As

expected, substantial nonlinearity is observed in the response of 45^{o} and 90^{o} specimens due to the high viscoelastic-viscoplastic effects and a remarkable amount of interphase and matrix damage. In contrast, the 0^{o} specimen response is much stiffer than the response of 45^{o} and 90^{o} specimens because of the higher probability of fibers oriented in the loading direction. The interphase and matrix damages are supposed to be the primary cause for the nonlinearity in the 0^{o} stress-strain response. The overall stress-strain behavior is captured with sufficient accuracy for the 0^{o} and 45^{o} configurations. For the 90^{o} specimen, the MT-TFA predictions coincide with the experimental values at the initial loading stages but predict stiffer response than the experimental results with continued applied strains. The deviation of the response at large applied strains at 90^{o} specimen can be attributed to several factors that are not taken into account in the present work, such as the inelastic flow involving a beginning of finite strains and rotations or the hydrostatic stress effect commonly admitted in the polymeric materials. Nevertheless, the obtained results demonstrate the model's capability to capture properly the strain rate effect, the damage evolution in the interphase and matrix phases, as well as the viscoelastic-viscoplastic deformation.

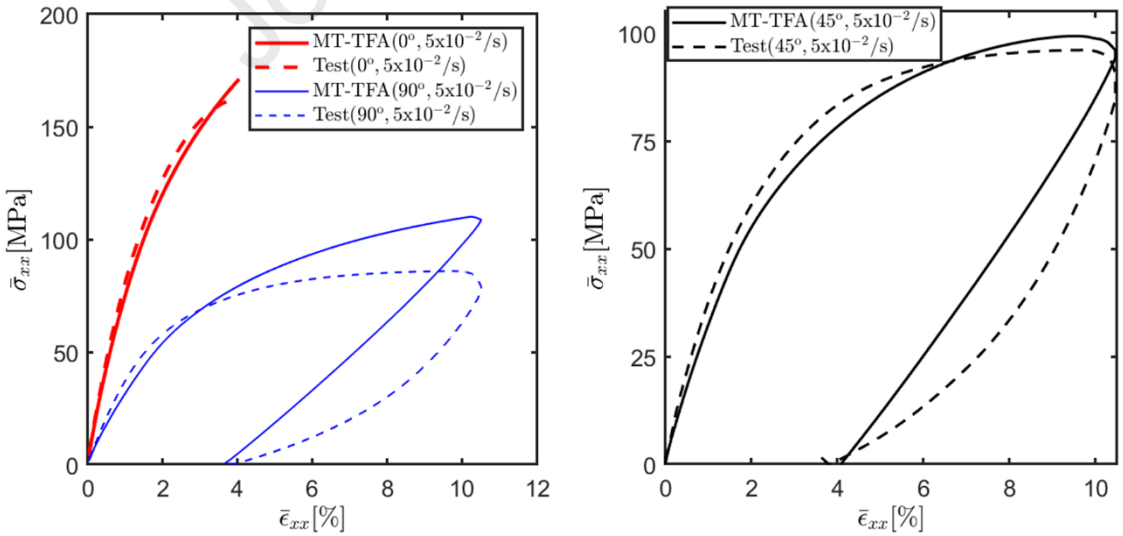

(a) $5 \times 10^{-2}/\mathrm{s}$

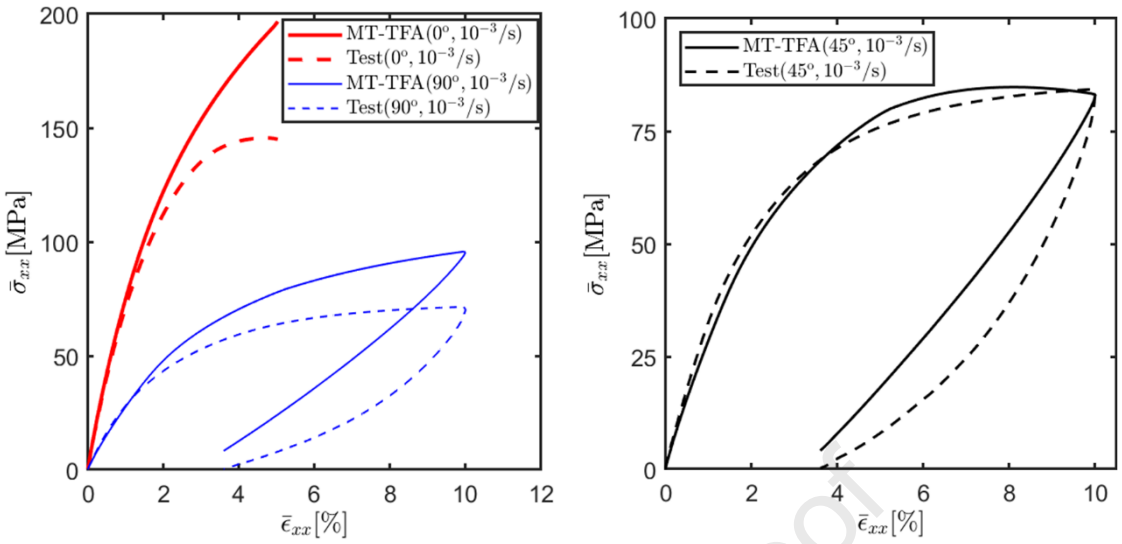

(b) $1\times 10^{-3}/\mathrm{s}$

Figure 10 Calibration of the interphase material based on uniaxial macroscopic load/unload stress-strain curves at strain rates of (a) $5\times 10^{-2}/\mathrm{s}$; (b) $1\times 10^{-3}/\mathrm{s}$

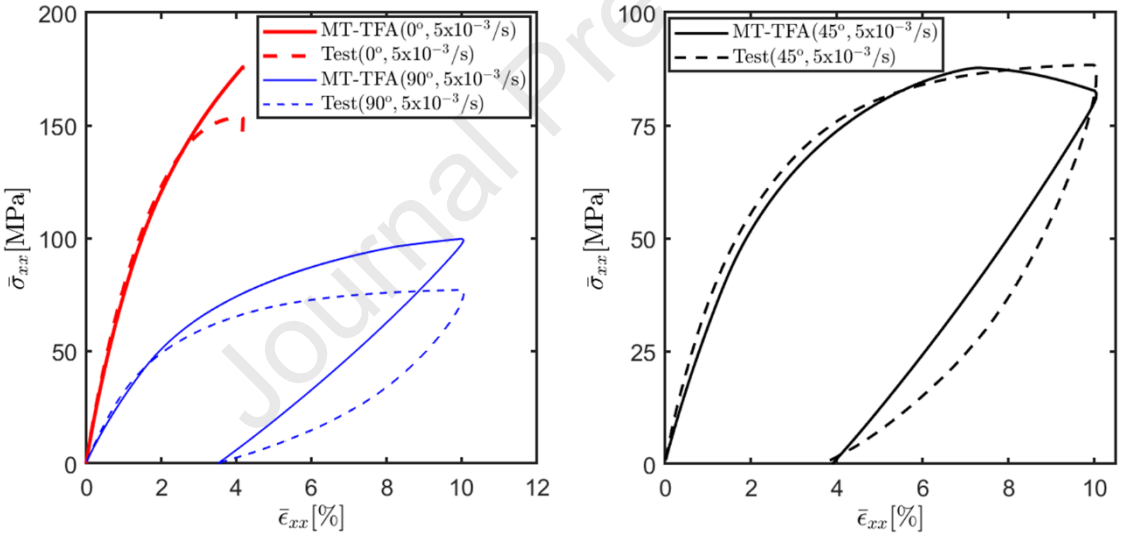

(a) $5\times 10^{-3}/\mathrm{s}$

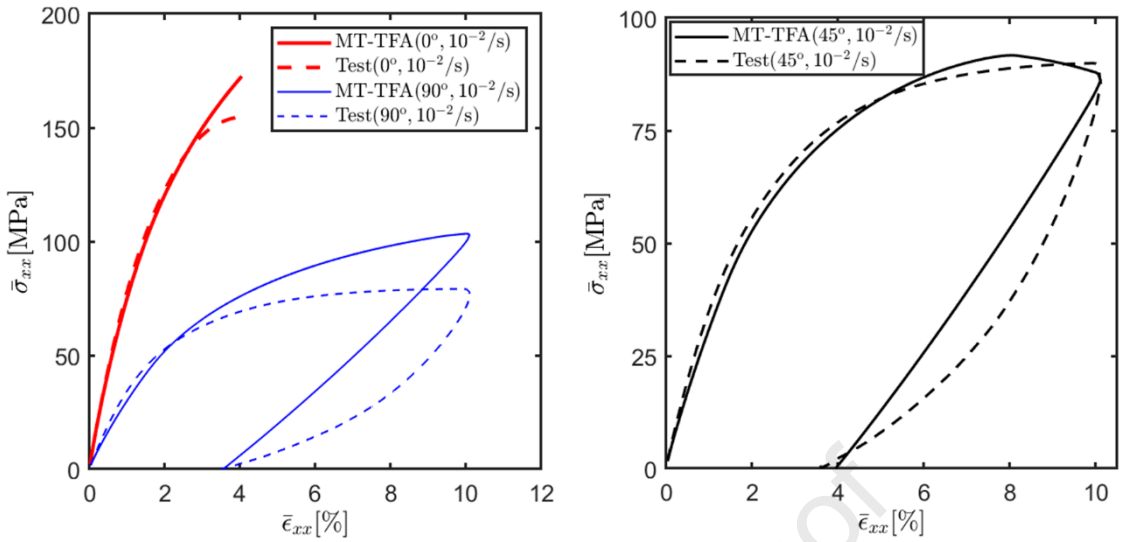

(b) $1\times 10^{-2}/\mathrm{s}$

Figure 11 Comparison of the macroscopic stress-strain curves of PA66/GF35 generated using the MT-TFA approach with the deduced interphase parameters with the experimental data at strain rates of (a) $5\times 10^{-3}/\mathrm{s}$; (b) $1\times 10^{-2}/\mathrm{s}$

To get more evidence on the validity of the proposed MT-TFA damage framework, comparison between the simulated and test stress-strain response is presented in Figure 12 for PA66/GF30 composite system containing 30% fiber content, which corresponds to 15.5% fiber volume fraction. For this material system, the uniaxial monotonic loading tests are performed on 0°, 15°, 30°, 45°, 60° and 90° orientations with respect to the mold-flow injection direction at a constant strain rate of $1\times 10^{-3}/\mathrm{s}$. It should be pointed out that the fiber orientation density function of the PA66/GF35 is directly used for the PA66/GF30 since they are both manufactured using the injection molding methods and their fiber volume contents are close. Similar conclusions for analytical/experimental correlations can be drawn for the PA66/GF30 composite systems as in the PA66/GF35.

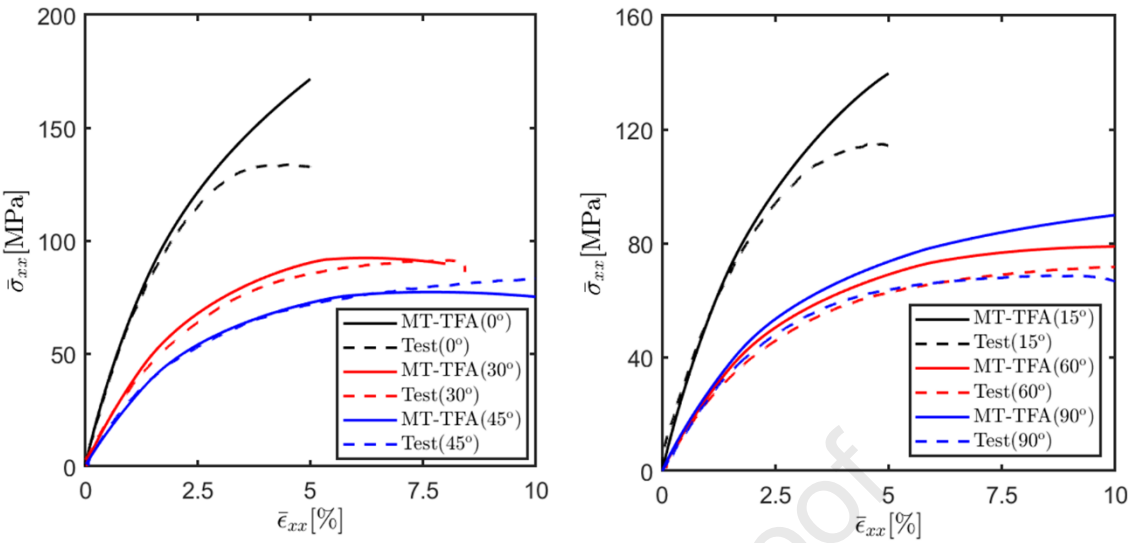

Figure 12 Comparison between the macroscopic stress-strain curves of PA66/GF30 generated using the MT-TFA approach with the deduced interphase parameters and the experimental data at strain rate of $1\times 10^{-3}/\mathrm{s}$

5 Oligocyclic Loading

The predictive capabilities of the extended Mori-Tanaka TFA approach are further validated upon simulating the oligocyclic response of the randomly-oriented PA66/GF35 composites based on the interphase and matrix parameters identified in the previous subsection. It should be pointed out that accurate simulating the oligocyclic response is more difficult relative to the uniaxial monotonic loading cases, as the effect of damage is the dominant mechanism in controlling the overall composite response with increasing load cycle. An additional complication is the fact that interactions between the viscoelasticity-viscoplasticity and the damage in different phases are more important during cyclic loading. Hence, it provides a very rigorous test and critical assessment of the accuracy of the proposed technique. The incremental load/unload cyclic tests are carried on the 0^{o}, 45^{o}, and 90^{o} PA66/GF35 specimens until fracture, at two averaged strain rates of $10^{-2}/\mathrm{s}$ and $10^{-3}/\mathrm{s}$, respectively.

Using the derived interphase properties, the extended MT-TFA simulations based on the actual fiber orientations of the PA66/GF35, subjected to oligocyclic loading, are compared with

the corresponding experimental response. Figures 13-15 illustrate the MT-TFA-experimental correlations for the 0^o, 45^o, and 90^o off-axis specimens at two average strain rates: $10^{-3}/\text{s}$ and $10^{-2}/\text{s}$, respectively. It should be noted that at the considered load level, macroscopic fracture occurs after 5 loading/unloading cycles in the case of 0^o specimen. In the case of 45^o, and 90^o specimens, the oligocyclic loading can be performed up to 10 cycles. Overall, the predicted response of the 0^o specimen exhibits good accordance with the experimental data in the nonlinear region, although a slight deviation may be observed after two cycles. Similar comments can be applied to the 90^o specimen. In contrast, the predicted hysteresis response of the 45^o specimen closely matches the experimental results of the entire deformation history, including the actual magnitudes and the observed trends as a function of the applied strains. It is important to note that at the early stage of the loading, there is virtually no difference between the MT-TFA predictions and experimental results for all the three orientations. The nonlinearity of the response is mainly attributed to the damage development, as the viscoelastic-viscoplastic effects are less significant at this load range. This suggests that the developed damage constitutive model is capable of offering realistic damage predictions.

The viscoelastic-viscoplastic and damage framework captures well the first loading/unloading cycles that present narrow hysteresis loops. However, with the increase of inelastic strain, the model is less accurate compared to the experiments, which exhibit larger hysteresis loops. Indeed, the later loops take progressively a banana shape due to the fiber/matrix friction at the debonded interfaces combined with the viscoelasticity nature of the polyamide matrix. Despite this issue, the agreement between the present predictions and testing data is still encouraging for the possible use of the proposed technique for predicting the nonlinear stress-strain behavior with progressive damage evolution in this class of materials.

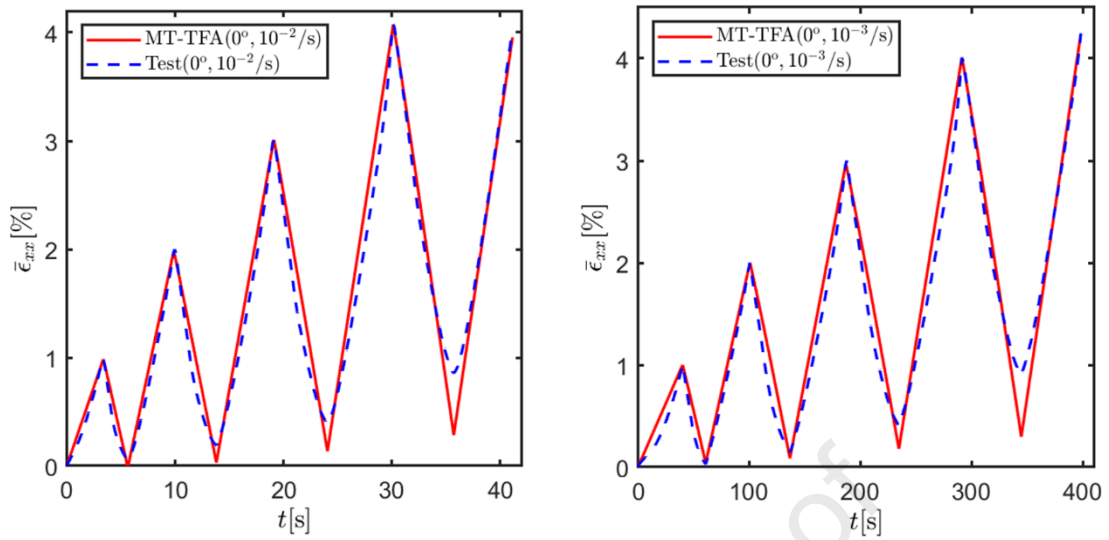

(a) Strain VS time

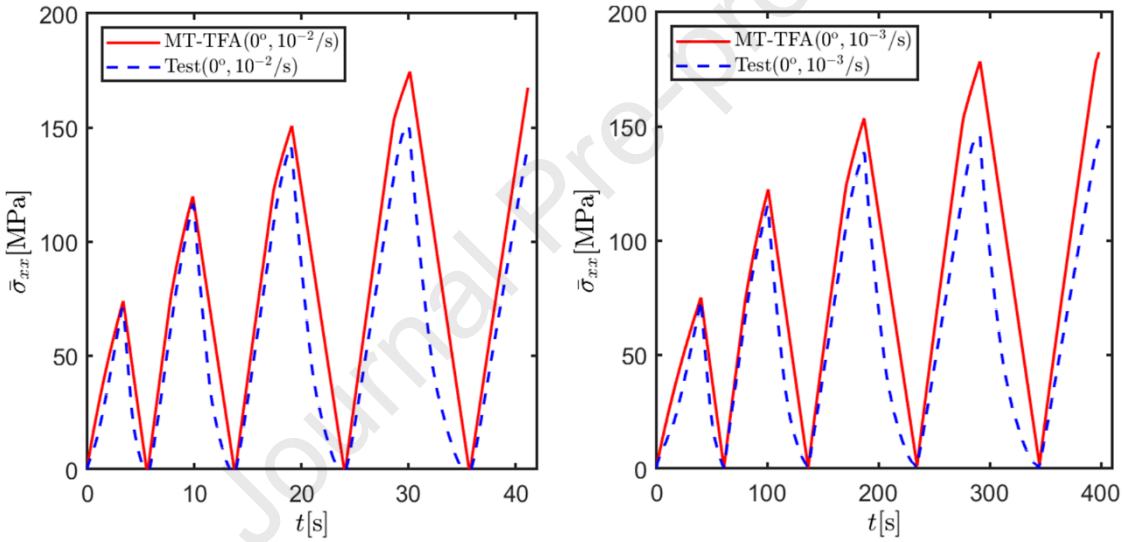

(b) Stress VS time

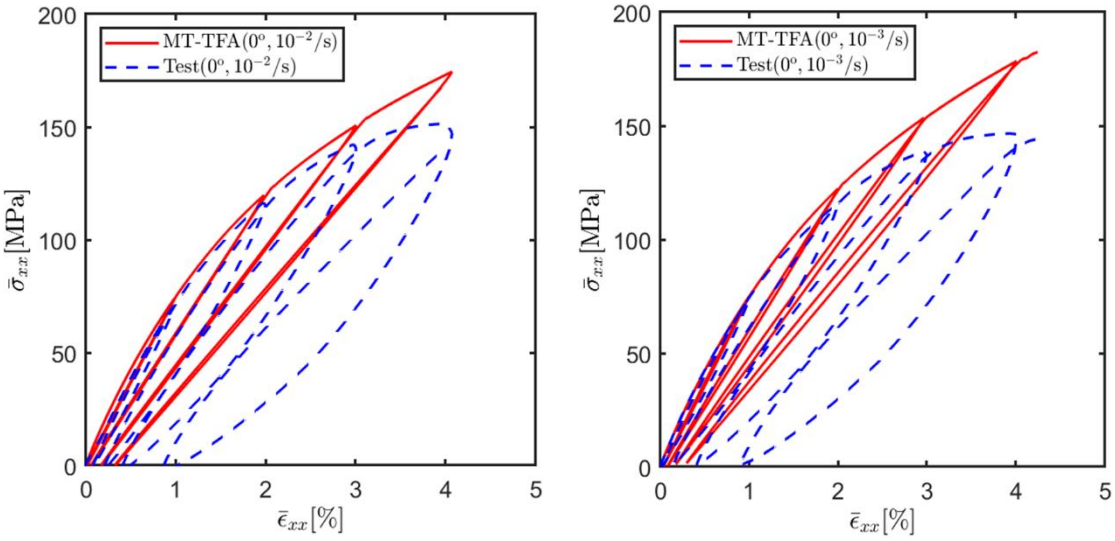

(c) Stress VS strain

Figure 13 Comparison of the cyclic response of the 0^o PA66/GF35 composites generated by the modified MT-TFA approach and the experimental data at averaged loading rates of $10^{-2}/\mathrm{s}$ (left) and $10^{-3}/\mathrm{s}$ (right), respectively

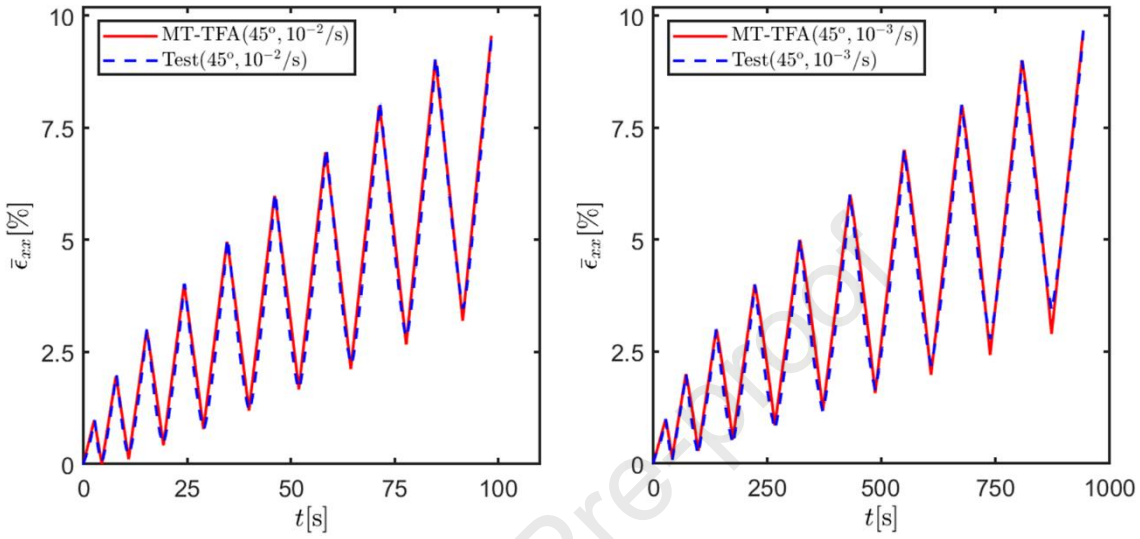

(a) Strain VS time

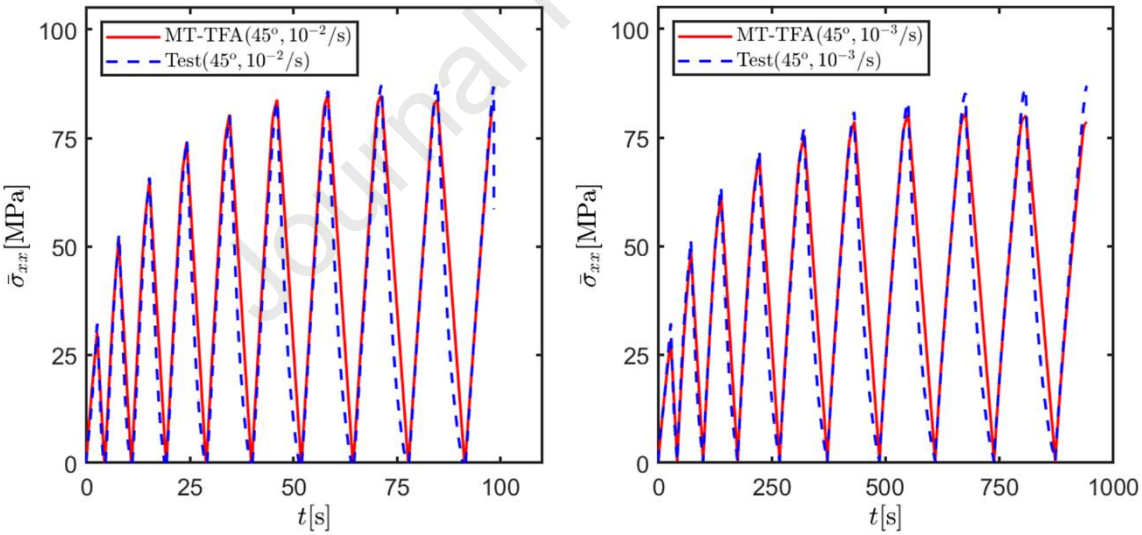

(b) Stress VS time

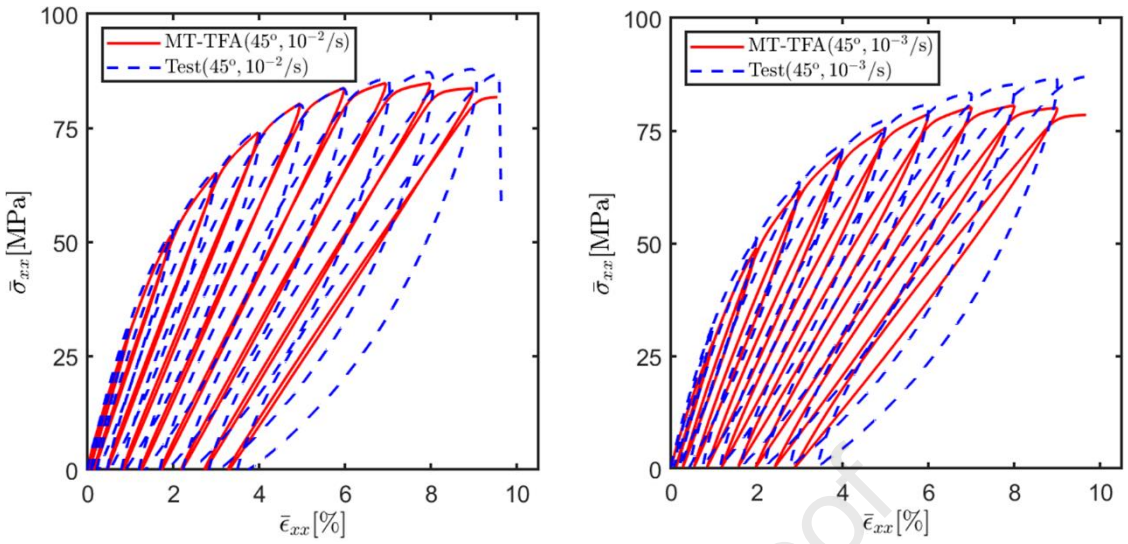

(c) Stress VS strain

Figure 14 Comparison of the cyclic response of the 45^{o} PA66/GF35 composites generated by the modified MT-TFA approach against the experimental data at averaged loading rates of $10^{-2}/\mathrm{s}$ (left) and $10^{-3}/\mathrm{s}$ (right), respectively

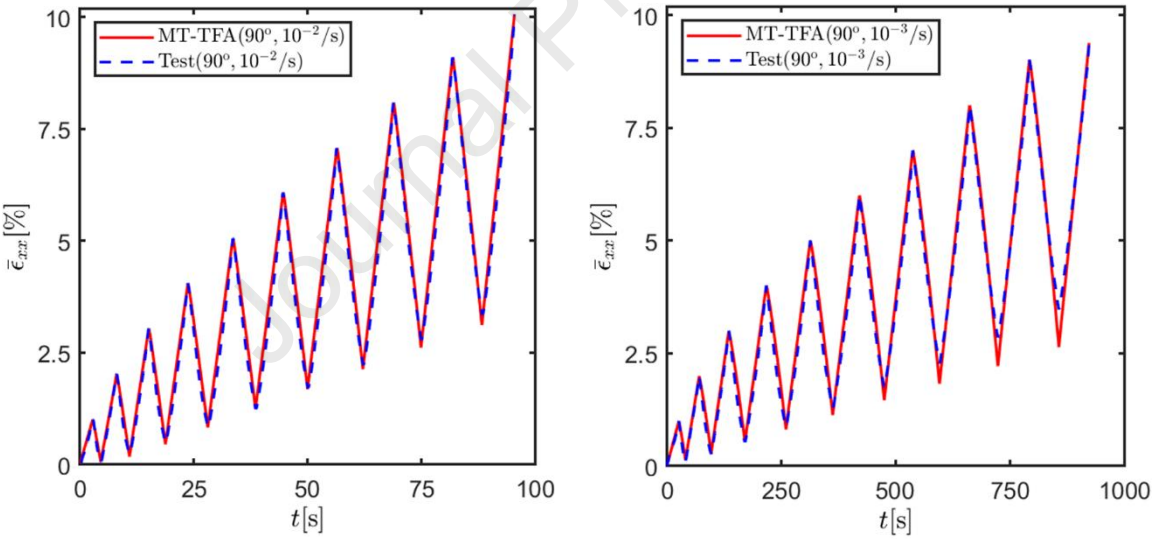

(a) Strain VS time

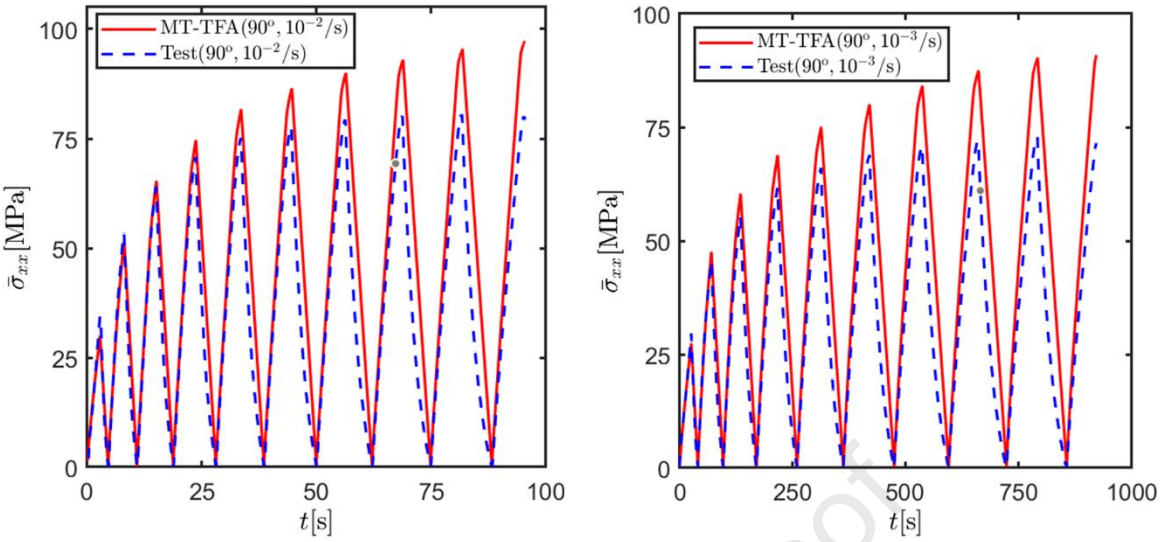

(b) Stress VS time

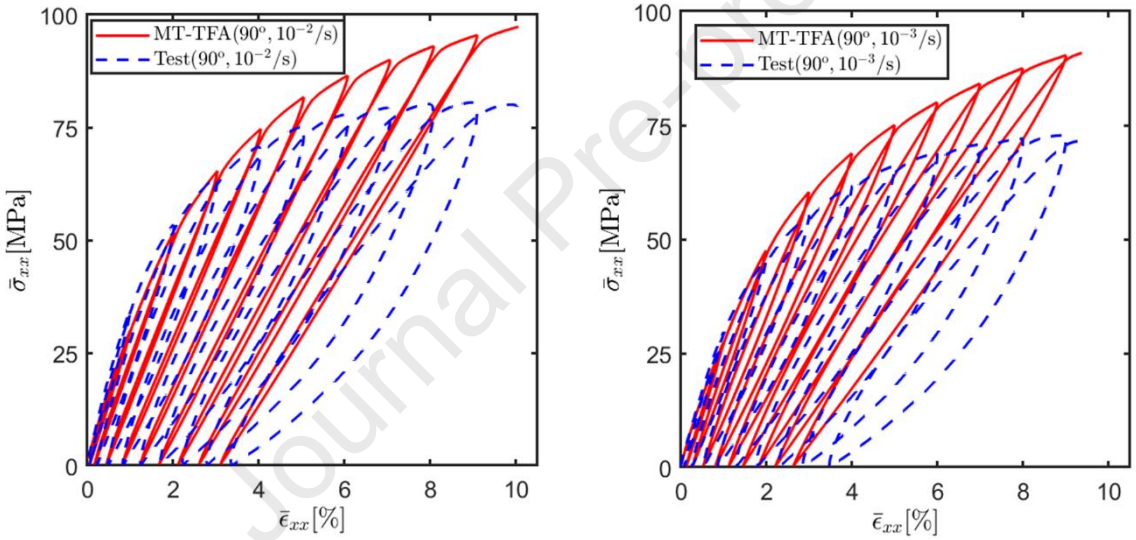

(c) Stress VS strain

Figure 15 Comparison of the cyclic response of the 90^{o} PA66/GF35 composites generated by the modified MT-TFA approach and the experimental data at averaged loading rates of $10^{-2}/\mathrm{s}$ (left) and $10^{-3}/\mathrm{s}$ (right), respectively

Figure 16 presents the corresponding damage evolution in the selected interphases and the matrix phase, γ_c and d, for the 0^{o}, 45^{o}, and 90^{o} specimens subjected to oligocyclic loading conditions. As anticipated, the damage evolutions in the interphase and matrix phases of the considered composites are completely different. They initiate from the interphase and then propagate through the polyamide matrix, which are supported by the experiment observations by

Arif et al. (2014a). Indeed, the interphase discrete damage γ_c accumulation is more rapid at the early stage of loading and the rate of the interphase damage formation decreases gradually with time. It is also observed that damage in both matrix and interphase is always increasing or remains constant, which is in accordance with the second principle of thermodynamics through Clausius Duhem inequality (Praud et al., 2017b). This figure also confirms the micro damage-induced global nonlinear stress-strain response at the early loading stages. In general, the microcracks initiate in the interphase and develop rapidly at the early loading stages while the matrix damage is not or less activated. Since the ductile damage is assumed to be proportional to accumulated viscoplastic strains, as shown in Table 1, the viscoplastic strains are not significant either. Therefore, the interphase degradation is the primary cause of the observed nonlinearity in the stress-strain response at the early loading stages.

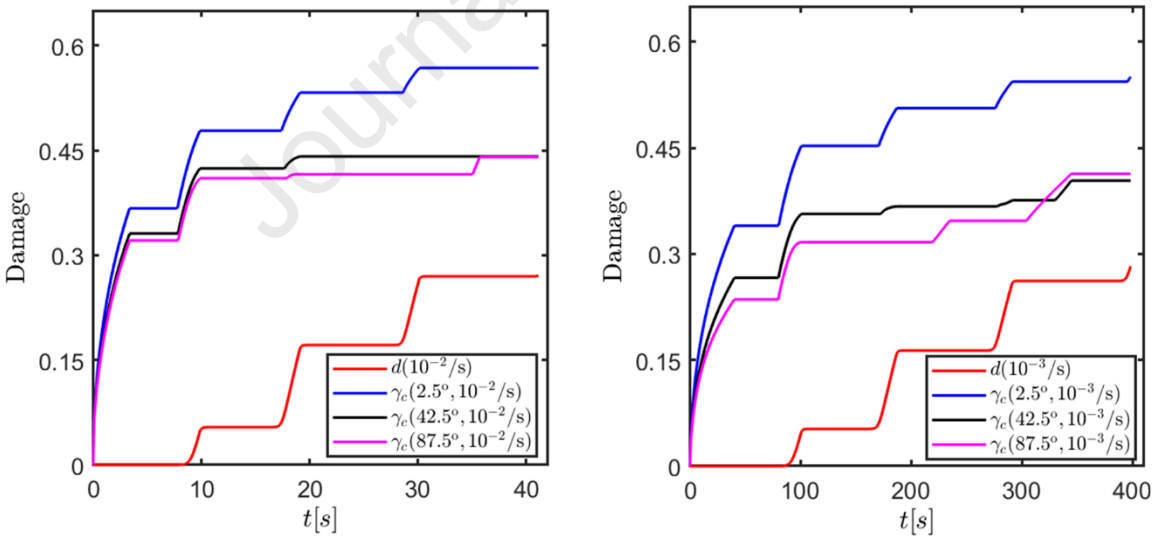

(a) 0^o

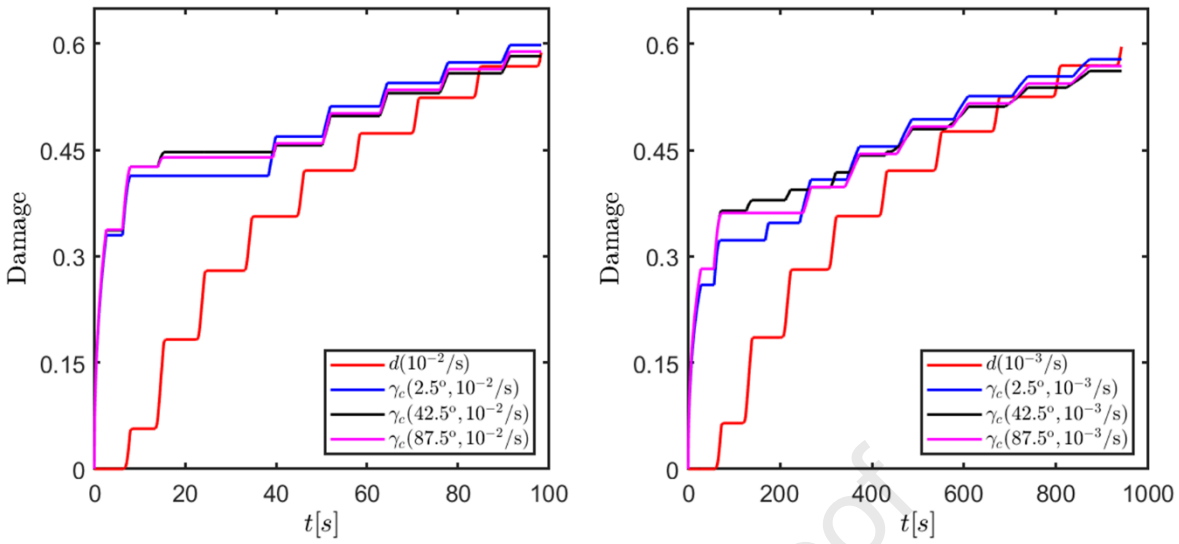

(b) 45°

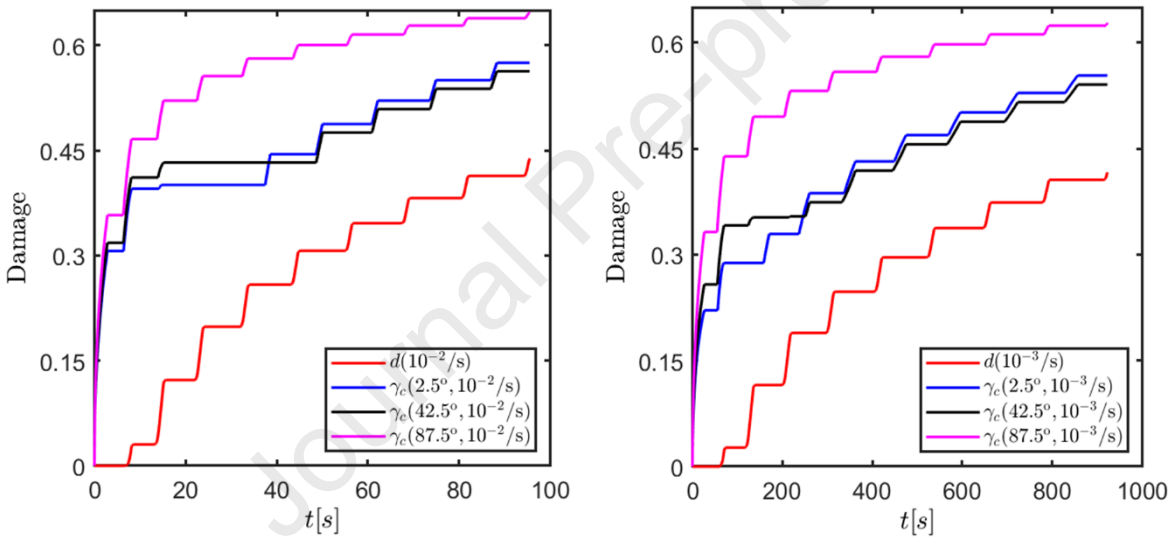

(c) 90°

Figure 16 Comparison of matrix ductile damage d and selected interphase damage γ_c as a function of time for three off-axis PA66/GF35 composites at averaged loading rates of $10^{-2}/\mathrm{s}$ (left) and $10^{-3}/\mathrm{s}$ (right), respectively. It is noted that the interphase orientation is given with respect to the $\bar{X}_2 - \bar{X}_3$ plane

Finally, comparison of the composite's effective "apparent" stiffness normalized by the initial values $\bar{E}_{xx}/\bar{E}^{o}_{xx}$ in the global coordinate systems obtained from unloading branches is presented in Figure 17. Very little data are readily available in the open literature concerning the stiffness reduction of the short fiber-reinforced polyamide composites during the oligocyclic loading, which is a good indicator that quantifies the overall damage evolution in composite

structures. Some differences are observed in the case of 45^{o} and 90^{o} specimens due to the errors in the evaluation of the initial stiffness. Nonetheless, the basic trends for stiffness reduction in experiments are seen to be captured by the modified MT-TFA model.

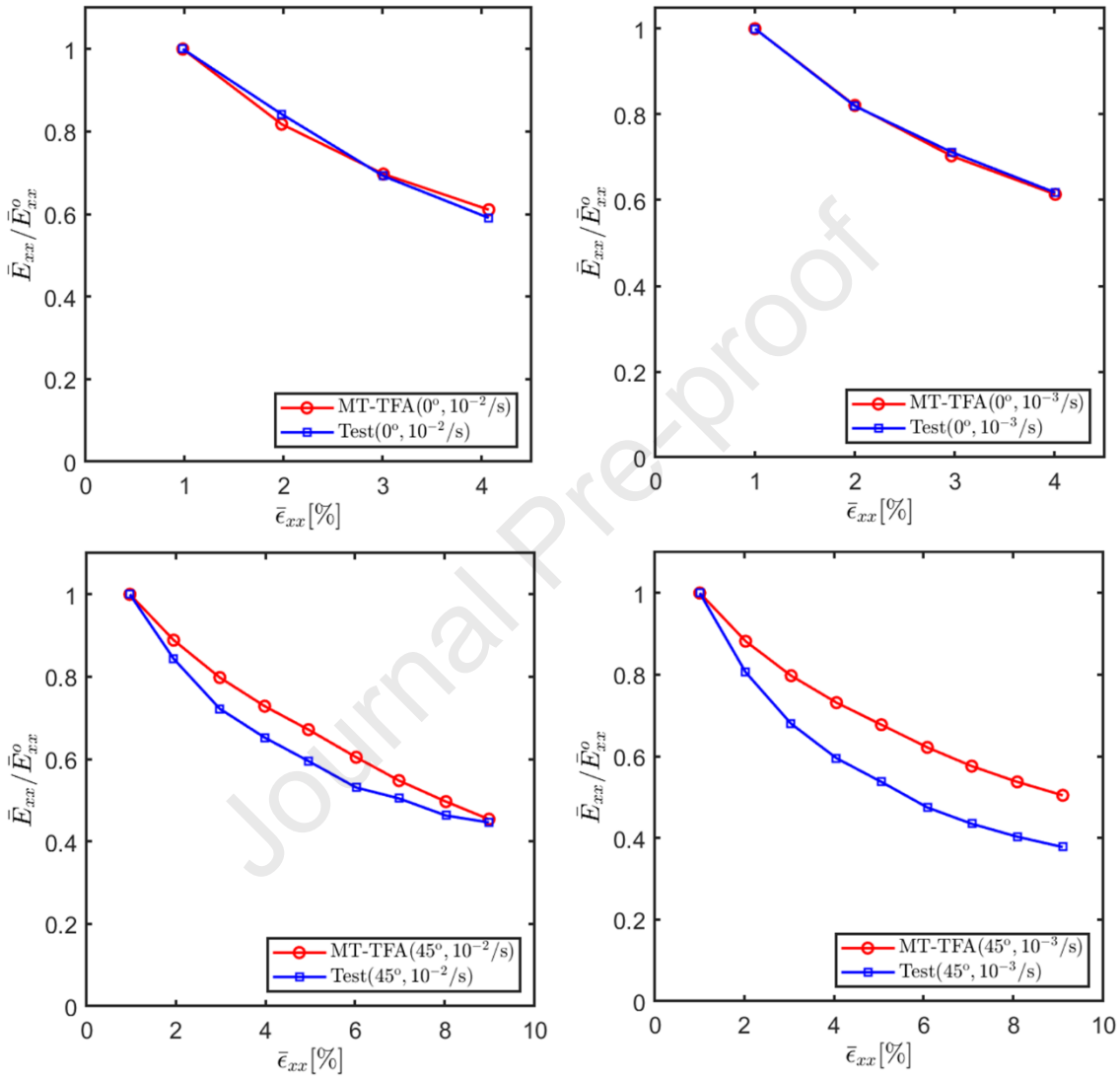

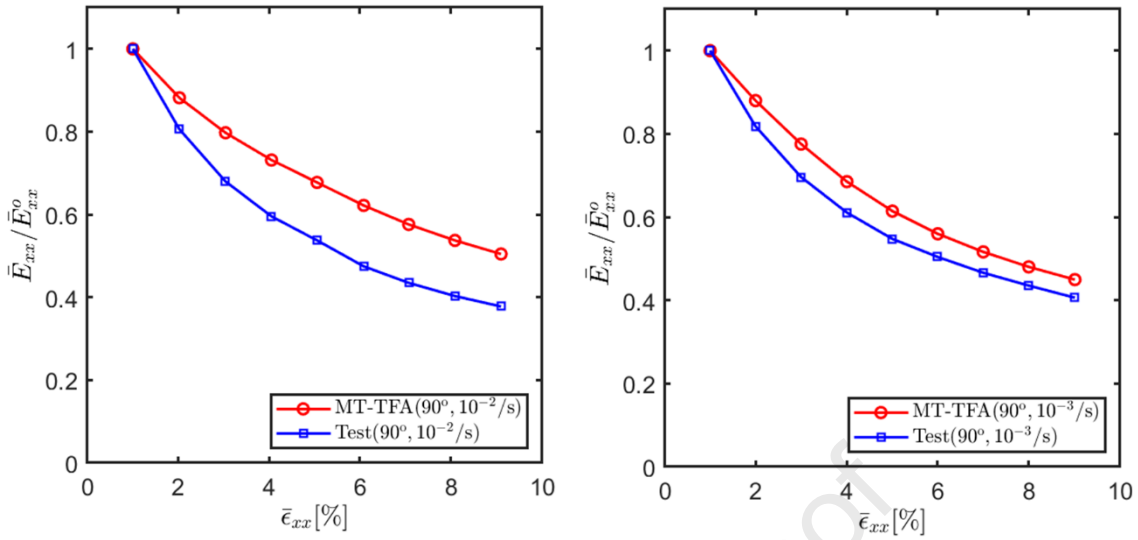

Figure 17 Comparison of the stiffness reduction $\bar{E}_{xx}/\bar{E}^{o}_{xx}$ for the cyclic loading obtained by the MT-TFA approach and experimental results at averaged loading rates of 10^{-2}/s (left) and 10^{-3}/s (right), respectively

6. Summary and Conclusion

Characterizing the response of thermoplastic composites continues to be an active and important area of research. The present work attempts to present an extended mean-field approach, based on the modified Mori-Tanaka and TFA techniques, to describe the experimentally-observed multi-mechanism inelastic deformation of short glass-fiber reinforced polyamide composites, under various loading conditions. In particular, the matrix inelastic behavior is simulated by a phenomenological model consisting of four Kelvin-Voigt branches and a viscoplastic branch, which is coupled with ductile damage. The interphase is described using a discrete damage model, wherein the microcrack/void initiation and growth follow the Weibull probabilistic function. The ability to incorporate the actual fiber arrangement and the ability to simulate different inelastic deformation and damage mechanisms at phase level make the developed techniques unique among the presently available micromechanics approaches.

The parameters of the developed models are calibrated using a minimum amount of experimental data obtained from uniaxial loading paths. The subsequent successful simulation of

the oligocyclic response of PA66/GF35 composites with three off-axis loading orientations at two loading rates, based on the deduced parameters, demonstrates the potential of the developed technique in accurately mimicking the response of polyamide composites under complex loading paths. The progressive interphase and matrix damage under various loading paths are also presented in support of the predictive capabilities of the extended MT-TFA approach. The numerical simulations indicate that local damage modes are induced by interfacial debonding in the vicinity of the reinforcements, followed by propagating through the matrix phase, which is consistent with the experimental observations.

Since the response of the polyamide is affected by the environmental conditions, it is imperative to incorporate a fully coupled thermo-hygro-damageable-mechanical phase constitutive model to address the temperature and moisture effects on the polyamide composite response. The extension to simulate the high-cycle fatigue damage by incorporating the cycle-jump techniques is also a worthwhile pursuit given the demonstrated accuracy of the present mean-field approach.

References

Advani, S.G., Tucker III, C.L., 1987. The use of tensors to describe and predict fiber orientation in short fiber composites. Journal of rheology 31, 751-784.

Ammar, A., Leclerc, W., Guessasma, M., Haddar, N., 2021. Discrete element approach to simulate debonding process in 3D short glass fibre composite materials: Application to PA6/GF30. Composite Structures 270, 114035.

Arif, M.F., Meraghni, F., Chemisky, Y., Despringre, N., Robert, G., 2014a. In situ damage mechanisms investigation of PA66/GF30 composite: Effect of relative humidity. Composites Part B: Engineering 58, 487-495.

Arif, M.F., Saintier, N., Meraghni, F., Fitoussi, J., Chemisky, Y., Robert, G., 2014b. Multiscale fatigue damage characterization in short glass fiber reinforced polyamide-66. Composites Part B: Engineering 61, 55-65.

Barral, M., Chatzigeorgiou, G., Meraghni, F., Léon, R., 2020. Homogenization using modified Mori-Tanaka and TFA framework for elastoplastic-viscoelastic-viscoplastic composites: Theory and numerical validation. International Journal of Plasticity 127, 102632.

Barthélémy, J.F., Giraud, A., Sanahuja, J., Sevostianov, I., 2019. Effective properties of ageing linear viscoelastic media with spheroidal inhomogeneities. International Journal of Engineering Science 144, 103104.

Boudet, J., Auslender, F., Bornert, M., Lapusta, Y., 2016. An incremental variational formulation for the prediction of the effective work-hardening behavior and field statistics of elasto-(visco)plastic composites. International Journal of Solids and Structures 83, 90-113.

Brassart, L., Stainier, L., Doghri, I., Delannay, L., 2012. Homogenization of elasto-(visco) plastic composites based on an incremental variational principle. International Journal of Plasticity 36, 86-112.

Charalambakis, N., Chatzigeorgiou, G., Chemisky, Y., Meraghni, F., 2018. Mathematical homogenization of inelastic dissipative materials: a survey and recent progress. Continuum Mechanics and Thermodynamics 30, 1-51.

Chatzigeorgiou, G., Charalambakis, N., Chemisky, Y., Meraghni, F., 2016. Periodic homogenization for fully coupled thermomechanical modeling of dissipative generalized standard materials. International Journal of Plasticity 81, 18-39.

Chatzigeorgiou, G., Charalambakis, N., Chemisky, Y., Meraghni, F., 2018. Thermomechanical behavior of dissipative composite materials. Elsevier.

Chatzigeorgiou, G., Meraghni, F., 2019. Elastic and inelastic local strain fields in composites with coated fibers or particles: Theory and validation. Mathematics and Mechanics of Solids 24, 2858-2894.

Chen, Q., Chatzigeorgiou, G., Meraghni, F., 2021a. Extended mean-field homogenization of viscoelastic-viscoplastic polymer composites undergoing hybrid progressive degradation induced by interface debonding and matrix ductile damage. International Journal of Solids and Structures 210-211, 1-17.

Chen, Q., Wang, G., Chen, X., Geng, J., 2017. Finite-volume homogenization of elastic/viscoelastic periodic materials. Composite Structures 182, 457-470.

Chen, Q., Wang, G., Pindera, M.-J., 2018. Homogenization and localization of nanoporous composites-A critical review and new developments. Composites Part B: Engineering 155, 329-368.

Chen, Q., Zhu, J., Tu, W., Wang, G., 2021b. A tangent finite-volume direct averaging micromechanics framework for elastoplastic porous materials: Theory and validation. International Journal of Plasticity 139, 102968.

Chen, Y.H., Aliabadi, M.H., 2019. Micromechanical modelling of the overall response of plain woven polymer matrix composites. International Journal of Engineering Science 145, 103163.

Cruz-González, O.L., Rodríguez-Ramos, R., Otero, J.A., Ramírez-Torres, A., Penta, R., Lebon, F., 2020. On the effective behavior of viscoelastic composites in three dimensions. International Journal of Engineering Science 157, 103377.

Despringre, N., Chemisky, Y., Bonnay, K., Meraghni, F., 2016. Micromechanical modeling of damage and load transfer in particulate composites with partially debonded interface. Composite Structures 155, 77-88.

Desrumaux, F., Meraghni, F., Benzeggagh, M.L., 2000. Micromechanical modelling coupled to a reliability approach for damage evolution prediction in composite materials. Appl Compos Mater 7, 231-250.

Drago, A.S., Pindera, M.-J., 2008. A locally exact homogenization theory for periodic microstructures with isotropic phases. Journal of Applied Mechanics 75, 051010

Dvorak, G.J., 1992. Transformation field analysis of inelastic composite materials. Proceedings of the Royal Society of London. Series A: Mathematical and Physical Sciences 437, 311-327.

Dvorak, G.J., Benveniste, Y., 1992. On transformation strains and uniform fields in multiphase elastic media. Proceedings of the Royal Society of London. Series A: Mathematical and Physical Sciences 437, 291-310.

Eshelby, J.D., 1957. The determination of the elastic field of an ellipsoidal inclusion, and related problems. Proceedings of the royal society of London. Series A. Mathematical and physical sciences 241, 376-396.

Gavazzi, A., Lagoudas, D., 1990. On the numerical evaluation of Eshelby's tensor and its application to elastoplastic fibrous composites. Computational mechanics 7, 13-19.

He, Z., Pindera, M.-J., 2021. Locally exact asymptotic homogenization of viscoelastic composites under anti-plane shear loading. Mechanics of Materials 155, 103752.

Hessman, P.A., Riedel, T., Welschinger, F., Hornberger, K., Böhlke, T., 2019. Microstructural analysis of short glass fiber reinforced thermoplastics based on x-ray micro-computed tomography. Composites Science and Technology 183, 107752.

Hine, P.J., Gusev, A.A., 2019. Validating a micromechanical modelling scheme for predicting the five independent viscoelastic constants of unidirectional carbon fibre composites. International Journal of Engineering Science 144, 103133.

Huang, H.-B., Huang, Z.-M., 2020. Micromechanical prediction of elastic-plastic behavior of a short fiber or particle reinforced composite. Composites Part A: Applied Science and Manufacturing 134, 105889.

Huang, H., Talreja, R., 2006. Numerical simulation of matrix micro-cracking in short fiber reinforced polymer composites: Initiation and propagation. Composites Science and Technology 66, 2743-2757.

Huang, Z.-M., 2020. Constitutive relation, deformation, failure and strength of composites reinforced with continuous/short fibers or particles. Composite Structures, 262, 113279.

Huang, Z.-M., Guo, W.-J., Huang, H.-B., Zhang, C.-C., 2021a. Tensile strength prediction of short fiber reinforced composites. Materials 14, 2708.

Huang, Z.-M., Wang, L.-s., Jiang, F., Xue, Y.D., 2021b. Detection on matrix induced composite failures. Composites Science and Technology 205, 108670.

Kaddour, A., Hinton, M., Smith, P., Li, S., 2013. Mechanical properties and details of composite laminates for the test cases used in the third world-wide failure exercise. Journal of Composite Materials 47, 2427-2442.

Krairi, A., Doghri, I., Schalnat, J., Robert, G., Van Paepegem, W., 2019. Thermo-mechanical coupling of a viscoelastic-viscoplastic model for thermoplastic polymers: Thermodynamical derivation and experimental assessment. International Journal of Plasticity 115, 154-177.

Lahellec, N., Suquet, P., 2007. On the effective behavior of nonlinear inelastic composites: I. Incremental variational principles. Journal of the Mechanics and Physics of Solids 55, 1932-1963.

Launay, A., Maitournam, M.H., Marco, Y., Raoult, I., Szmytka, F., 2011. Cyclic behaviour of short glass fibre reinforced polyamide: Experimental study and constitutive equations. International Journal of Plasticity 27, 1267-1293.

Lemaitre, J., Chaboche, J.-L., 1994. Mechanics of solid materials. Cambridge university press.

Mao, R.-S., Huang, Z.-M., Wang, Z.-W., 2021. Predicting strength of a unidirectional composite containing interface crack. Composites Science and Technology, 207, 108665.

Mercier, S., Molinari, A., 2009. Homogenization of elastic–viscoplastic heterogeneous materials: Self-consistent and Mori-Tanaka schemes. International Journal of Plasticity 25, 1024-1048.

Moulinec, H., Suquet, P., 1998. A numerical method for computing the overall response of nonlinear composites with complex microstructure. Computer methods in applied mechanics and engineering 157, 69-94.

Müller, V., Böhlke, T., 2016. Prediction of effective elastic properties of fiber reinforced composites using fiber orientation tensors. Composites Science and Technology 130, 36-45.

Mura, T., 1987. Mechanics of elastic and inelastic solids, Micromechanics of Defects in Solids. Martinus Nijhoff Publishers Dordrecht.

Otero, J.A., Rodríguez-Ramos, R., Guinovart-Díaz, R., Cruz-González, O.L., Sabina, F.J., Berger, H., Böhlke, T., 2020. Asymptotic and numerical homogenization methods applied to fibrous viscoelastic composites using Prony's series. Acta Mechanica 231, 2761-2771.

Peng, X., Tang, S., Hu, N., Han, J., 2016. Determination of the Eshelby tensor in mean-field schemes for evaluation of mechanical properties of elastoplastic composites. International Journal of Plasticity 76, 147-165.

Praud, F., Chatzigeorgiou, G., Bikard, J., Meraghni, F., 2017a. Phenomenological multi-mechanisms constitutive modelling for thermoplastic polymers, implicit implementation and experimental validation. Mechanics of Materials 114, 9-29.

Praud, F., Chatzigeorgiou, G., Chemisky, Y., Meraghni, F., 2017b. Hybrid micromechanical-phenomenological modelling of anisotropic damage and anelasticity induced by micro-cracks in unidirectional composites. Composite Structures 182, 223-236.

Praud, F., Chatzigeorgiou, G., Meraghni, F., 2021. Fully integrated multi-scale modelling of damage and time-dependency in thermoplastic-based woven composites. International Journal of Damage Mechanics 30, 163-195.

Rodríguez-Ramos, R., Berger, H., Guinovart-Díaz, R., López-Realpozo, J.C., Würkner, M., Gabbert, U., Bravo-Castillero, J., 2012. Two approaches for the evaluation of the effective

properties of elastic composite with parallelogram periodic cells. International Journal of Engineering Science 58, 2-10.

Simo, J., Hughes, T., 1998. Interdisciplinary applied mathematics. Mechanics and Materials, Computational Inelasticity. Springer-Verlag, New York.

Song, Z., Peng, X., Tang, S., Fu, T., 2020. A homogenization scheme for elastoplastic composites using concept of Mori-Tanaka method and average deformation power rate density. International Journal of Plasticity, 128, 102652.

Tikarrouchine, E., Benaarbia, A., Chatzigeorgiou, G., Meraghni, F., 2021. Non-linear FE2 multiscale simulation of damage, micro and macroscopic strains in polyamide 66-woven composite structures: Analysis and experimental validation. Composite Structures 255, 112926.

Tu, W., Chen, Q., 2020. Evolution of interfacial debonding of a unidirectional graphite/polyimide composite under off-axis loading. Engineering Fracture Mechanics, 230, 106947.

Wei, X., Li, D., Xiong, J., 2019. Fabrication and mechanical behaviors of an all-composite sandwich structure with a hexagon honeycomb core based on the tailor-folding approach. Composites Science and Technology 184, 107878.

Wei, X., Wu, Q., Gao, Y., Xiong, J., 2020. Bending characteristics of all-composite hexagon honeycomb sandwich beams: experimental tests and a three-dimensional failure mechanism map. Mechanics of Materials 148, 103401.

Weihull, W., 1951. A statistical distribution function of wide applicability. Journal of Applied Mechanics 18, 290-293.

Wu, L., Noels, L., Adam, L., Doghri, I., 2013. A combined incremental-secant mean-field homogenization scheme with per-phase residual strains for elasto-plastic composites. International Journal of Plasticity 51, 80-102.

Zhu, Y.T., Blumenthal, W.R., Lowe, T.C., 1997. Determination of non-symmetric 3-d fiber-orientation distribution and average fiber length in short-fiber composites. Journal of Composite Materials 31, 1287-1301.

HIGHLIGHTS

- A probabilistic micromechanics damage framework is proposed, based on the modified Mori-Tanaka method and Transformation Field Analysis,
- The first time that a modified Mori-Tanaka TFA approach that involves multi-deformation mechanisms and integrates the actual material microstructure is developed for short glass-fiber reinforced polyamide composites,
- The developed approach considers several deformation and damage mechanisms simultaneously. Namely, the matrix is described by the viscoelastic-viscoplastic model coupled with ductile damage. The fiber/matrix debonding is characterized by void creation and accumulation. The progressive degradation of the load transfer is introduced through a reduction of the effective fiber length,
- The developed approach is extensively validated against the experimental data under monotonic and oligocyclic loading paths. Progressive matrix and interphase damage are compared in support of the modified MT-TFA technique's capabilities to capture the experimentally observed damage mechanisms.

Declaration of interests

☒ The authors declare that they have no known competing financial interests or personal relationships that could have appeared to influence the work reported in this paper.

☐The authors declare the following financial interests/personal relationships which may be considered as potential competing interests: